Synthesis and Optical studies of Pure and La/Mn co-substituted $BiFeO_3$ thin films

By

Asra Babar

DEPARTMENT OF PHYSICS

QUAID-I-AZAM UNIVERSITY

ISLAMABAD, PAKISTAN

2021-2023

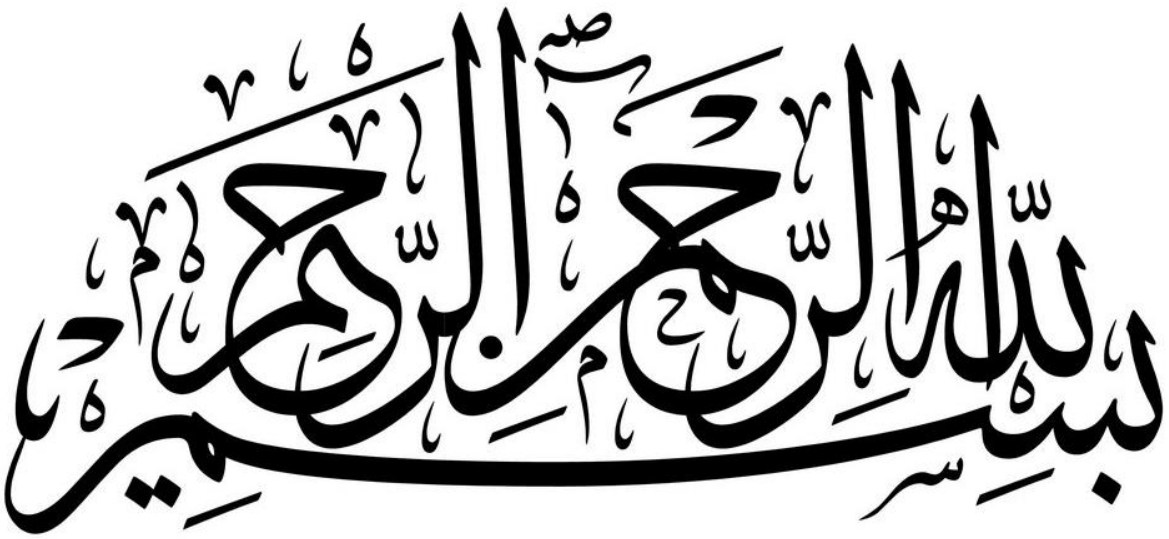
بسم الله الرحمن الرحيم

This work is submitted as a dissertation

In partial fulfillment of the requirement for the degree of

MASTER OF PHILOSOPHY

IN

PHYSICS

To the

Department of Physics

Quaid-i-Azam University

Islamabad, Pakistan

2021-2023

CERTIFICATE

This is to certify that the experimental work in this dissertation has been carried out by ***Asra Babar*** under my supervision in the Superconductivity and Magnetism Lab, Department of Physics, Quaid-i-Azam University, Islamabad, Pakistan.

Supervisor:

Prof. Dr. Ghulam Hassnain Jaffari

Department of physics

Quaid-i-Azam University

Islamabad, Pakistan

Submitted Through:

Prof. Dr. Kashif Sabeeh

Chairman

Department of Physics

Quaid-i-Azam University

Islamabad, Pakistan.

To

My Parents

Acknowledgements

First of all I would like to express my gratefulness to Almighty Allah, who gives me the strength and energy to fulfill this research work. His continuous grace and mercy was with me throughout my life and even more during the tenure of my research. Without his blessings, this achievement would not have been possible.

With deep regards and profound respect, I take this opportunity to express my deep sense of gratitude and indebtedness to my supervisor ***Dr. Ghulam Hassnain Jaffari,*** for his supervision, valuable suggestions and help that inspired me to complete this research work. He guided me all the way with his characteristic wisdom and patience and bore all my limitations with utmost affection. Indeed, without his unfathomable support this work would not have been possible.

I would like to express my sincere gratitude to ***Dr. Fiza Mumtaz*** for her invaluable guidance and support throughout my journey. Her wisdom, experience, and mentorship have played a pivotal role in shaping my professional growth. I am truly fortunate to have had the opportunity to learn from such a dedicated and accomplished senior.

I want to express my heartfelt thanks to ***Musfira Aqeel*** and ***Sumbal Amin*** for their instrumental role in this thesis. Their wisdom, guidance, and tireless efforts have not only enriched the research but have also been a source of inspiration for me as a researcher. I would like to pay my gratitude to my lab fellows especially ***Umm-e-Habiba***.

My parents ***Zaheer Ud Din Babar*** and ***Tasneem Waqar*** are truly amazing. My motivation comes from their love and faith. Words cannot express the depth of my gratitude for their unconditional love and support, but I am indebted to them for their support and love throughout this journey. I feel pleasure to acknowledge my siblings, my lovely brother ***Muhammad Huzaifa Naseer*** and caring sisters ***Esha Zaheer*** and ***Muqadas Rubab.***

I want to take a moment to thank ***Ammara Kalsoom*** from the bottom of my heart for her friendship. We don't frequently meet people who are as sincere, kind, and encouraging as she is, therefore I count myself quite lucky to have her in my life.

ABSTRACT

Bismuth ferrite (BFO) is a very well-known multiferroic material due to the existence of multiferroic properties at room temperature and is a promising candidate for magnetoelectric applications which makes it very useful for the potential devices. However, it is difficult to synthesize single phase BFO and control leakage current, which restricts its use in commercial applications. Additionally, because of its polycrystalline and porous structure and high leakage current levels, this material is difficult to use commercially. To solve this problem, scientists have been developing new approaches for the synthesis of multiferroic materials based on BFO. Therefore, to achieve the pure phase and to reduce the Bi^{3+} volatilization issue with minimized porosity and leakage current BFO is doped with La/Mn at A-site and B-site respectively. By using chemical solution deposition technique BFO thin films have been prepared on FTO glass substrates in present work. This thesis presents a detailed investigation of pure, La^{3+} substituted, Mn^{3+} substituted and La^{3+}-Mn^{3+} co-substituted BFO thin films. Detailed study of structural and optical properties have been investigated. It is expected that substitution of La^{3+} for Bi^{3+} can control the Bi^{3+} volatilization. In studies, it can be found that the substitutions of dopants at A and B-site of BFO induce dominant effects in structure and optical properties of BFO. Structure of the prepared films are investigated using XRD and Raman analysis. Optical properties and bandgap studies of all the pure and doped compositions have been carried out within the spectral range of 1.5 eV to 5 eV. Within this spectral range, two *d-d* transitions and two charge transfer transitions were observed. The change of transitions by addition of dopants at A-site and B-site were studied in detail by calculating various parameters using Tanabe Sugano Diagrams. Identifying the role of dopants in reduction of bandgap values is also part of the present study.

Table of Contents

List of figures

Chapter 1 Introduction and Background

Chapter 2 Experimental Techniques

Chapter 3 Synthesis and Structural Characterization

Chapter 4 Results and Discussion

List of Tables

Chapter 1 Introduction and Background

Ferrites are divided into four groups which depend upon their crystal structure such as Spinel, Garnet, Ortho and Hexagonal ferrites. In Ortho Ferrites, $TbMnO_3$ and $BiFeO_3$ are the most well-known multiferroic materials because of the presence of ferro-electricity and magnetism at room temperature, which are much suitable to be used as memory cores of digital devices. Multiferroics materials have two or more order parameters at the same time and attract more interest because of the existence of the Magneto electric coupling (ME). By changing electric field (*E*) in ME, magnetic states can be controlled and the other way round [2].

$BiFeO_3$ (BFO) is one of the interesting multiferroic materials due to the presence of ferroelectricity and ferromagnetism at room temperature. BFO has the ability to play a role in memory devices, semiconductors sensors and photo catalytic activities etc. $BiFeO_3$ being singly phase is challenging in order to develop due to the existence of different types of impurity phases appear due to bismuth excess phases. These issues should be resolved in order to obtain $BiFeO_3$ based high quality multifunctional devices. It is investigated that phase purity of BFO can be performed by using different synthesis procedures or doped it with suitable substituent. Thin films of BFO are prepared to reduce leakage current in order to resolve these issues and to obtain phase stability of BFO by doping it with La^{3+} at A-site and Mn^{3+} at B-site. The purpose of this research work is to study the effect of La^{3+} and Mn^{3+} substitution on Optical and structural properties of $BiFeO_3$ thin films.

1.1 History of Multiferroic

Complex metal oxides are interesting for physicists particularly among the domains of material science and condensed matter physics. They reveal a wide range of remarkable features, including high-temperature superconductivity [3] , ferroelectricity [4], magnetism [5], tremendous magnetoresistance [6], piezoelectric [7], and more recently multiferroic attributes [5]. Because ferroelectric and ferromagnetic materials play an important role in modern day technologies, such as magnetic sensors, integrated circuits, fragile memory devices for data, and multiferroic solar cells etc. [8]. Applications for such materials in spintronics and magnetoelectronics seem to be promising.

Multiferroic materials are those materials that exhibit more than one ferroic property. Ferroic properties can be ferroelectric, ferro/anti-magnetic, and ferroelastic [9]. The word multiferroic was

first introduced by Schmidt. $BiFeO_3$ (BFO) is the considerable example of multiferroic materials that show long-range ferroelectric and ferromagnetic ordering at room temperature [10]. Magnetoelectric coupling (MEC) is another property of multiferroic materials in which polarization can be affected by applying a magnetic field, magnetization can be easily changed via the application of an electric field [11]. It has a rhombohedral unit cell comprised of two perovskite cells that were initially correlated in a pseudocubic [111] direction [12]. This chapter gives an overview of electronic transitions, multiferroic materials, optical and structural properties of solids. The chapter also describe Bismuth Ferrite (BFO) briefly which is currently being studied.

1.2 Electrical Conductivity in Solids

The conductivity that occurs from the movement of electrons or holes is referred as electronic conductivity. The conductivity of electrons and holes, respectively, is known as n-type conductivity and p-type conductivity. Due to additional electrons available for conduction, metals turn more electrically conducting. Pure ionic solids are insulators as they lack the ions needed for conduction. Crystal defects enhance electrical conductivity. Electrical conductivities of solids might vary between 10^{-20} to 10^{7} ohm^{-1} m^{-1}. Solids are grouped into three different categories based on their conductivities. Disparity in conductivity between conductors, insulators, and semiconductors (Dielectrics) has been brought to light with the aid of band theory.

1.2.1 Energy Bands of Solids

Based on their electrical parameters, band gap, and density of states, there are three distinct groups of materials which are following:

1. Insulators
2. Semiconductors and Dielectrics
3. Conductors

1.2.1.1 Insulators

Materials exhibiting a band gap that is large above 3 eV is referred as insulator. A wide gap in the band creates the vacant conduction band when electrons lack sufficient energy to penetrate the barrier. The conductivities for insulators vary between 10^{-10} and 10^{-20} $ohm^{-1}m^{-1}$. These include paper, glass, & wood.

1.2.1.2 Semiconductors and Dielectrics

Between conductors and insulators there exist materials which are called semiconductors. Semiconductors have electrical conductivity which lies in the range 10^{-6} and 10^{4} ohm^{-1} m^{-1}. Between the valence and conduction bands, they have an extremely small gap. Rising temperatures could result in an increase in conductivity. By gaining thermal energy, electrons can overcome the band gap energy. The conductivity of semiconductor materials can also be raised using ideal dopants**.**

1.2.1.3 Conductors

As there is no band gap separation in both valence and conduction bands, these materials possess high conductivity. Conductivities of these materials lie between 10^{4} and 10^{7} ohm^{-1} m^{-1}. Electrons are capable of moving freely and contribute to conduction. By raising the temperature, conductivity drops, leading the resistance to go up. Examples are Silver, Gold, and Copper. The insulator, semiconductor, and conductor band gaps are shown in figure 1.1.

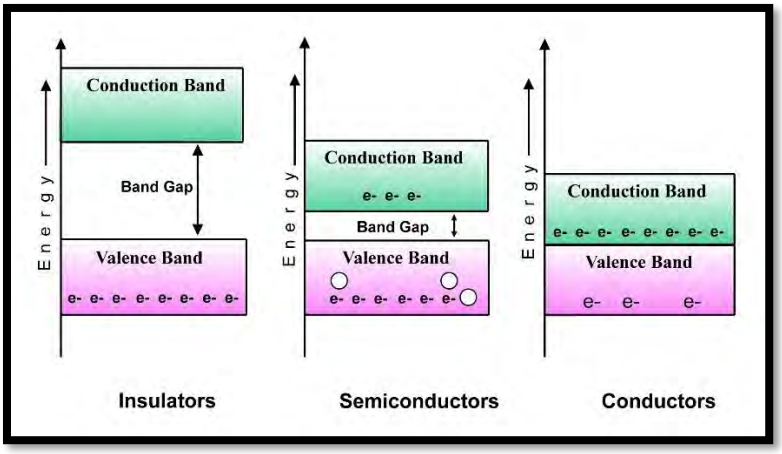

Figure 1.1: The Band Diagram of Insulator, Semiconductor, and Conductor.

1.3 Electronic Transitions

An electronic transition involves the shift of electrons from the state of lower energy to the higher energy level. Different selection rules especially these electronic transitions are subjected by Laporte selection rule, spin selection rule, and symmetry selection rule [13]. The *d-d* and charge transfer transitions are the most examined electronic transitions in materials [14].

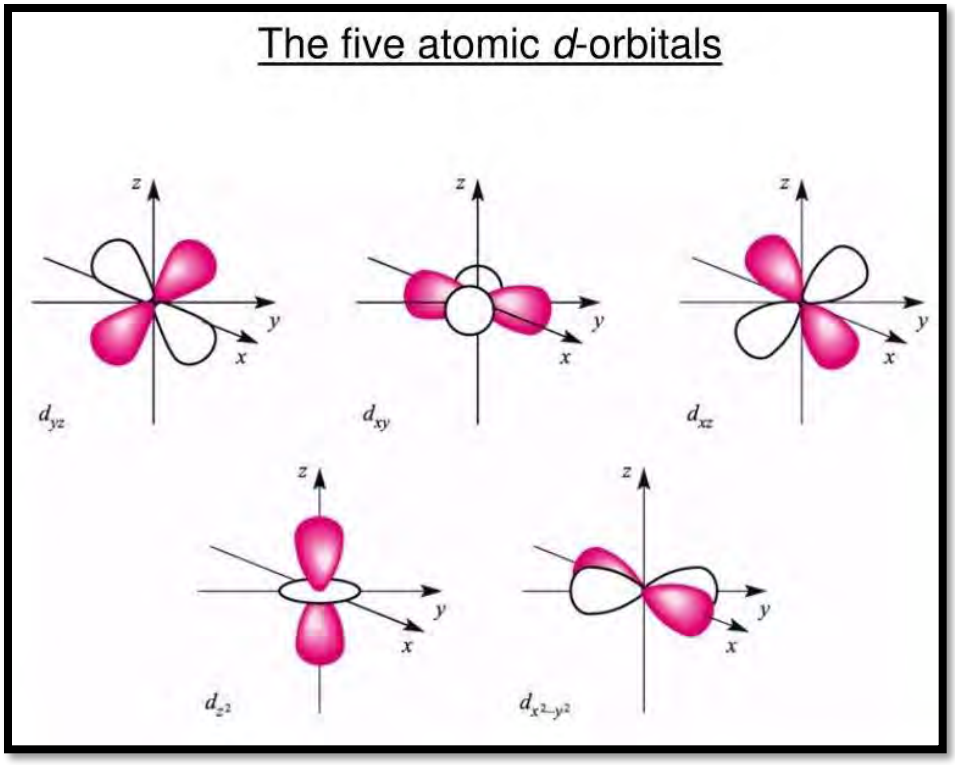

Figure 1.2: Degenerate *d*-orbital shapes.

1.3.1 *d-d* Transitions

The *d-d* transitions signify the shifting of electrons within a molecule's *d*-orbital. The concept of crystal field theory is used to understand *d-d* transitions. Five degenerate orbitals are found in an octahedron and in a transition metal with a tetrahedron at center, but they detach as a result of coulomb repulsion between an oxygen atom and the nearby filled p-orbital. Due to degeneracy of d-orbitals, two separate classes t_{2g} and e_g exist. When the d_{xy}, d_{yz} and d_{zx} orbitals in the t_{2g} and the $d_{x^2-y^2}$, and d_{z^2}, orbitals in the e_g orbitals have orientations aligned in x, y, and z axes, correspondingly, *d-d* transitions occur between the t_{2g} and e_g orbitals in octahedral complexes given in figure 1.2.

1.3.1.1 Crystal field splitting in an octahedral complex

The metal ion is encapsulated by six ligands in the octahedral compound, and electron repulsion between the ligand electrons and the electrons in the *d*-orbital is exposed. Although they point in the direction of the axes that correspond with the direction of the ligands, the d_{x2-dy2}, and d_{z2} orbitals results in increased repulsion. As a result, they are energized than the usual energy in

a spherical crystal field. However, because they are directed between the axes, d_{xy}, d_{yz}, and d_{zx} orbitals are less resistive.

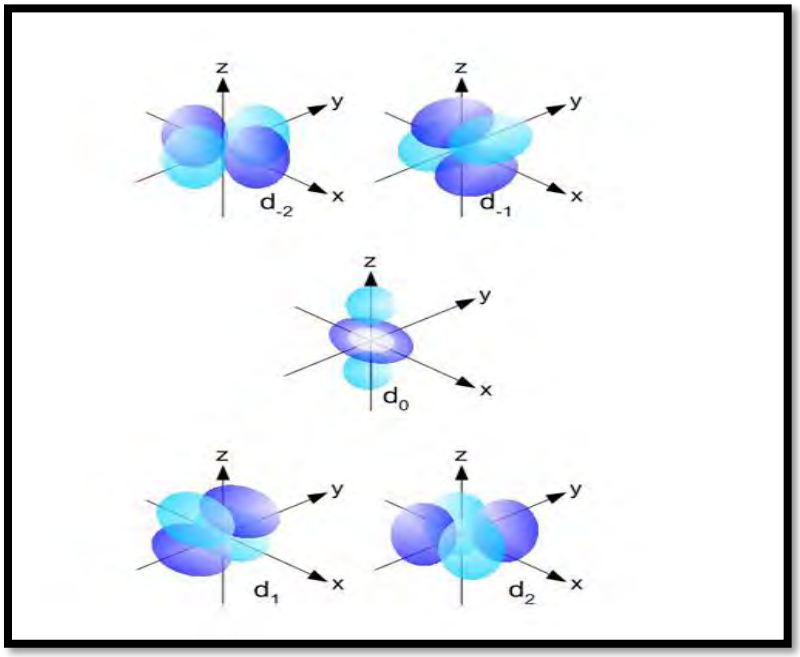

Figure 1.3: e_g and t_{2g} *d*-orbitals in crystal field.

The six ligand atoms in the octahedral cage did not influence all of the *d*-orbitals in the same fashion. Six oxygen ions are positioned at the corner of the octahedron in accordance with octahedral symmetry, and e_g orbitals point to the direction of each of these oxygen ions. These orbitals have considerably greater energy level than t_{2g} orbitals because of strong attraction in the *d*-electrons of the transition metal ions and electrons of ligand ions. Nevertheless, in the tetrahedral cage, as shown in figure 1.3, the e_g orbitals avoid the charge density imposed by the ligand atoms positioned at the corners of the tetrahedron and have a lower energy than the t_{2g} orbitals. The symbol represents the energy difference between these orbitals is Δ.

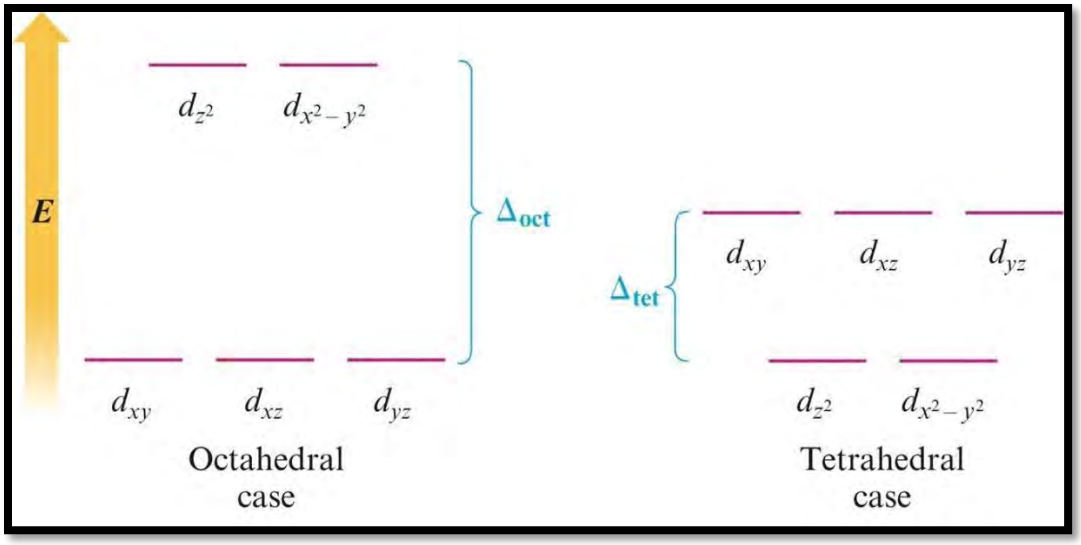

Figure 1.4: Octahedral and tetrahedral *d*-orbital splitting [15].

1.3.2 Charge transfer transitions

Charge transfer transition happens as significant quantities of an electronic charge that is transferred from a single aspect of a molecular entity known as the electron donor and other one is electron acceptor. Charge transfer bands between molecular orbitals (MO), which are usually made up of metals in nature, and ligand-dominated molecular orbitals are produced in transition metal complexes. The transition is known as a ligand-to-metal charge transfer (LMCT) if it arises between a MO and accepting ligand-like properties and MO possessing a metal-like property (figure 1.5 (a)). The band can be described as a metal-to-ligand charge transfer (MLCT) if the electrical charge is transferred from the metal-like MO to the ligand-like MO (figure 1.5 (b)). As a consequence, an MLCT enables the metal to oxidize, however an LMCT causes that metal center to decrease [16].

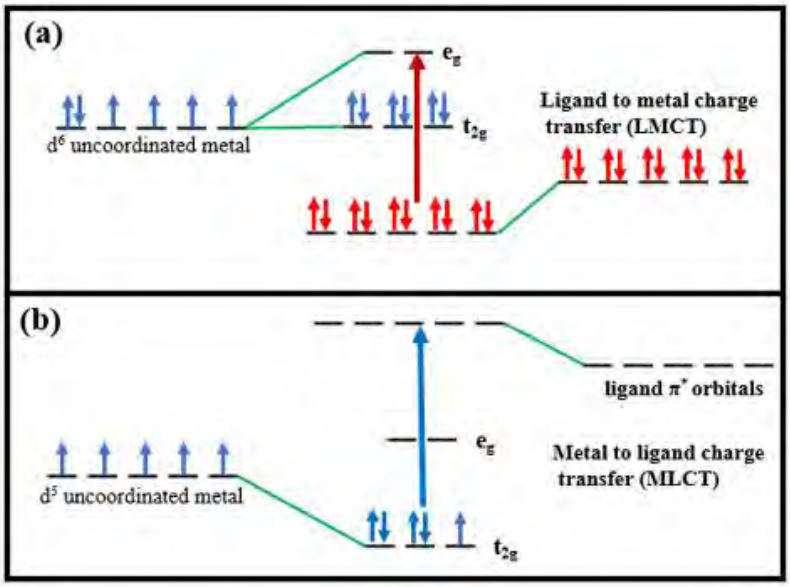

Figure 1.5: (a) Metal to ligand charge transfer involving d^5 octahedral complex (b) Ligand to metal charge transfer involving d^6 octahedral complex [17].

1.4 Multiferroics Materials and their Advantages

Multiferroics are captivating multifunctional materials in which simultaneous ferromagnetism and ferroelectricity are two examples of multiple ferroic orders [9]. Due to their rising prominence, multiferroic materials can also be created artificially in addition to being found in nature. One of the most significant varieties of multiferroics is the magnetoelectric multiferroic because it associates magnetic and electric properties. This is called Magnetoelectric coupling [23, 24]. Since ferromagnetism and ferroelectricity have different characteristics and properties, it is not easy to control one through the conjugate field of the other. In contrast, magnetization in magneto-electric coupling is caused by altering the elements of the electric field, and vice versa. On the other hand, magnetization and polarization are also brought about by strain in a material and are known as magnetoelasticity and ferroelasticity, respectively. In addition to having both ferroelectricity and ferromagnetism in one phase, multiferroic materials are significant because their combined parameters known as "magnetoelectric coupling" allow them to put to use in various devices [8, 25, 26]. Also Ferroelectric Random-Access Memories (FeRAM) have admirable characteristics with regard to non-volatility, Low energy consumption, outstanding density, quick writing speed, and long-lasting performance, but have slow readability. Ferromagnetic materials have fast readability but have slow writing speed and need a large amount

of energy (because of high coercivity). Materials with ferroelectric write and ferromagnetic read functionality would improve the writing speed and reduce the specific energy consumption.

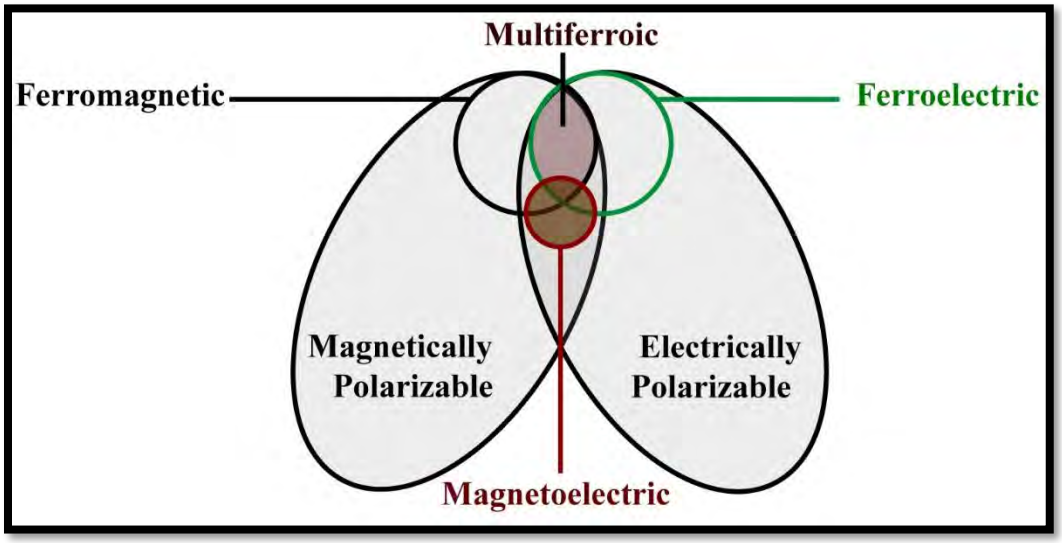

Figure 1.6: Representation of the relation between magnetoelectric and multiferroic [23].

1.5 Perovskite Structure

The perovskite substances has the name of Russian mineralogist Count Lev Alekseyevich von Perovski]16[. Perovskites fall within a broad family of crystals that share traits with $CaTiO_3$. The equation for perovskites is ABX_3. According to figure 1.7, a cube has an anion ('X') at the face centers and two cations ('A' and 'B') at the corners. A-site cations frequently have valences between +1 and +3, whereas B-site cations typically have valences between +3 and +6. The ionic radius of the A-site cation is typically greater than that of the B-site atoms in most perovskites, whereas the anion 'X' is primarily a fluorine or oxygen ion. Perovskites have drawn a lot of interest due to their electric, magnetic and multiferroic capabilities because of the association between spin, charge, and orbits in these materials]16[.

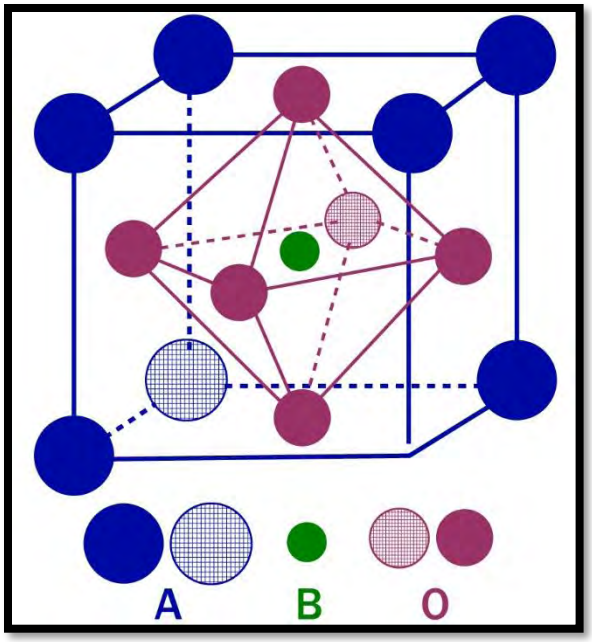

Figure 1.7: ABX_3 perovskite unit cell.

1.6 Literature Survey of Bismuth Ferrite ($BiFeO_3$)

1.6.1 Physical Properties

Due to the simplicity of their crystal structure and availability in a variety of compositions, perovskite are identical to it have served as a bedrock for the building of numerous useful materials. Research has been done extensively on bismuth ferrite ($BiFeO_3$), a multiferroic with a perovskite structure. The rarest single-phase multiferroic among many magnetoelectric (ME) materials is a BFO with an ABO_3-type perovskite structure. BFO is a well-known multiferroic material because of magnetoelectric coupling (ME) at normal temperature. It was initially synthesized in 1957 by Royen and Swars]27[. BFO has a strong saturation polarization (90 C/cm^2) and a modest ferromagnetism. With a value of (2.74 eV)]28[, it has a narrow bandgap. It depicts ferroelectric behavior at standard room temperature, with a Curie temperature of roughly 1103K and a Neel temperature of roughly 643K. According to reports, the perovskite structure of BFO can be recognized by an R3c space group and rhombohedral distortion in the plane at room temperature. At a wavelength of 62 nm, BFO exhibits G-type antiferromagnetism together with non-collinear spins and spiral spin structure.

Bi's single pair is responsible for the ferroelectric characteristics of the BFO, while Fe's partially filled *d*-orbital is responsible for magnetism [29, 30].

1.6.2 Crystal structure of BFO

Bi^{+3} a trivalent cation, can be found at the A-site of BFO, making it distinct from other perovskite structures which only have divalent cations, which includes rare earth metals. To comprehend BFO's multiferroic and magnetoelectric properties, one must first grasp its fundamental crystal structure. BFO at room temperature comprises a rhombohedrally deformed structure and an R3c space group perovskite structure [31]. Bi^{+3} cations have 6s electrons in their valence shell, and these electrons are reactive in terms of their spatial locations and electron energy bands. This reactivity may result in the formation of 6s lone pairs or covalent interactions with oxygen ions. While iron ions ($Fe^{+3)}$ interact via a super exchange mechanism to produce magnetic ordering within the BFO, the hybridization of the Bi^{+3} lone pair with the O^{2-}(2p orbital) causes Bi^{+3} to move from its centrosymmetric positions, which causes ferroelectric polarization to take place in a certain direction. [32, 33]. Figure 1.8 illustrates the structure of the BFO as well as the polarization direction. The lone pair process, in which displacement is induced by an A-site and magnetism is passed on by partially filled *d*-orbitals of B-site cations, is considered to be the origin of the simultaneous coexistence of ferroelectricity and magnetism in materials like $PbVO_3$, $BiMnO_3$, and $BiFeO_3$ [34, 35]. Figure 1.8 depicts the FeO_6 octahedra generated by the B-site Fe^{3+} ions in BFO. These octahedra are linked to each other by sharing their corners, yielding a perovskite (ABO_3) type $BiFeO_3$ structure.

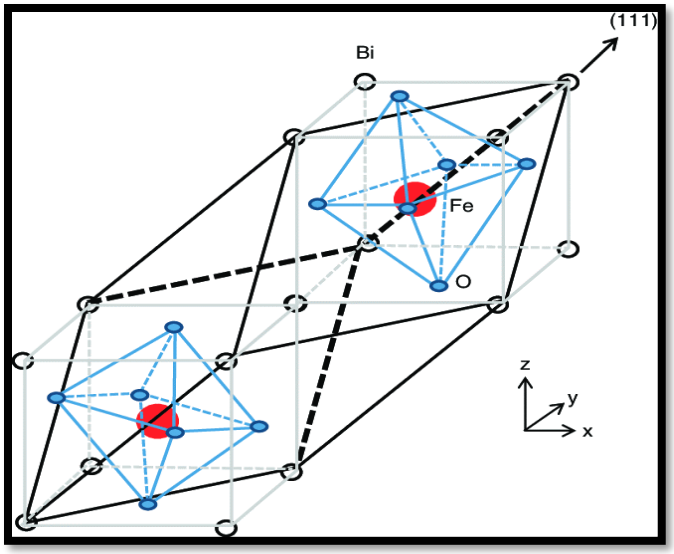

Figure 1.8: Schematic diagram of rhombohedral BFO cells.

1.6.3 Bismuth Ferrite thin films

Since its discovery in 1957, $BiFeO_3$ ceramic has played a crucial role in the fabrication of sensors [36], random-access memory devices [9, 37], and other products. However, the synthesis of BFO ceramics is difficult because of the volatilization of Bi^{+3} and oxygen vacancies, and as a result, various secondary phases emerge undergoing the sintering process. Furtherer, significant leakage current is seen as a result of the change in the valence state of iron, specifically Fe^{+3} and Fe^{+2}, as well as the production of oxygen vacancies, both of which can cause BFO ceramics' ferroelectric characteristics to decline. Therefore, replacing other ions for bismuth can improve the ferroelectric attributes of BFO ceramics [38]. According to published reports, Alkaline Earth metal substitution on the BFO's A-site can maintain the crystal structure and enhance ceramic's ferroelectric and ferromagnetic characteristics [12, 39-41]. Furthermore, the multiferroic characteristics of BFO strengthen and the crucial problems with BFO ceramics diminish when other elements are utilized in place of Fe on the B-site [42-44]. To lessen the generation of secondary phases and high leakage current, improved and novel synthesis techniques for the production of bulk BFO have been introduced. Bi and Fe oxides serve a purpose in the bulk BFO preparation process. It is possible for secondary phases like $Bi_2Fe_4O_9$, $Bi_{25}FeO_{40}$, and Bi_2O_3 to form. These secondary phases have been significantly diminished by making use of the right precursor oxides and more accurate chemical techniques. Since bulk BFO has a polycrystalline structure and an immense leakage current, it is difficult to attain intrinsic ferroelectric

characteristics [45, 46]. As a result, superior BFO thin films with reduced leakage current and improved ferroelectric response can be generated in comparison to BFO ceramics by choosing the correct fabrication techniques and maximizing synthesis parameters. BFO thin films have attracted a lot of attention due to their eventual use in new magnetoelectric devices and their function in fundamental magnetoelectric. In contrast to the challenging task with creating a BFO-based ceramic with exceptional ferroelectric qualities, thin BFO films are simple to construct. BFO thin films thus attract more attention. On SRO/STO substrates, the creation of a BFO thin film with a large P_r of 55 $\mu C\ cm^{-2}$ in 2003 reported by Wang *et al*. [47]. The very first example of such a high P_r in case of BFO led to sharp rise in the amount of research being conducted on BFO thin films. Epitaxial BFO film structure is modulated by the BFO film's thickness and epitaxial strain on various substrates so the structural phases of BFO thin films can include rhombohedral-like (R-like) phase, pseudocubic phase, tetragonal-like (T-like) phase and even fully strained tetragonal (T) phase. The creation of solid solutions or the insertion of additional components can also have a significant effect on the structure of thin films.

1.6.4 A-Site doping in BFO

In the achievement of pure phases doping of trivalent cations, like Lanthanides ($La^{+3,}$ Nd^{+3}, Gd^{+3}, Pr^{+3}, Sm^{+3}) and divalent cations like (Pb^{+2}, Ca^{+2} and Ba^{+2}), for bismuth displays good response. By using these doping, structural transitions also seen and ferroelectric properties have also been enhanced. Doping of rare-earth cations in BFO was reported in order to increase the magnetocrystalline anisotropy, which in turn makes its cycloidal spin structure unfavorable. By substituting a small amount of isovalent ion for Bi^{3+} aids to stabilize the $BiFeO_3$ phase. Considering doping of La for the BFO sample has been studied in contrast about the physical changes brought about by the isovalent substitution of bismuth cations, physical pro by isovalent substitution of bismuth cations (Bi^{+3}) for rare earth cations like La^{+3}($Bi_{1-x}La_xFeO_3$). It is frequently known that lanthanum (La) controls the growth of secondary phases and lowers leakage currents. In this study, an effective method for regulating the conductivity of multiferroic materials based on $BiFeO_3$ is provided with pure phase structure by co-doping with La and Mg at Bi and Fe site respectively [48, 49].

1.6.5 B-site doping in BFO

The magnetic property in the perovskite BFO is primarily brought about by the B-Site ions. For the existence of strong magnetoelectric coupling BFO should exhibit ferromagnetism but it is antiferromagnetic at room temperature and this property make it most studied material. Ni doping effects in BFO has been studied by Wang *et al.* [50] in which the magnetization of Ni-doped BFO enhances (0.8 emu/gm) greatly for Ni doping, concentration equal to 0.5%. Also by S. Chauhan *et al.* [51] and B. Dhanalakshmi *et al* [52]. Revealed how ferromagnetic properties improve when Mn doping in BiFeO3 rises. In Wenlong Liu *et al* [53]. On FTO glass substrates, thin films of both undoped and Mn-doped BFO were created, and the effects of Mn doping on the structure were examined. Mn doping also suppressed the oxygen vacancies. Doping on B-site (using Ni, Ti and Zn as dopant) singly seems unfriendly because of the presence of uncontrollable secondary phases [54, 55]. Hence it is expected that co-doping is expected to be interesting as far as the physical properties are concerned.

1.6.6 Co-doping in BFO

Rajasree Das *et al*. [56] reported that if we co-doped BFO with Ba^{+2} and Gd^{+3} ions possess improved magnetoelectric coupling coefficient, polarization, and high resistivity at room temperature. Benfang Yu *et al.* [57] examined how co-doping affected BFO using La^{+3} (15%) and V^{+5} (0-10%) and reported the formation of second phase in all samples but still the doping resulted in enhanced ferroelectric and anti-fatigue properties. BFO was also doped with La and V in a way keeping V concentration 3% and value of La varied from 5% to 20%, resulted in improvement of magnetic properties and reduced the leakage current [58]. This work by X.J. Xi *et al.* [59] suggest that in multiferroic materials based on pure-phase $BiFeO_3$, co-doping with La and Mg at Bi and Fe sites has proven to be an effective method for controlling conductivity. Impure phases are absent even in $La_{0.2}Bi_{0.8}Fe_{0.95}Mg_{0.05}O_3$ ceramics, and every sample maintains a rhombohedral structure.

1.6.7 Applications of BFO

BFO material has been widely utilized in spintronics, hardware, and photonics in view of its superior performance. BFO materials have a lot of potential for the design and development of new devices of multiferroic nature. Because of their magnetoelectric coupling, BFO's make it possible to write data using magnetism and store it as an electric field. Multiferroics can be used in both magnetic data storage (MS) and ferroelectric random-access memory (RAM) because of

their high coupling. Multiferroic devices explore the best features of conventional magnetic and ferroelectric random-access memories while consuming little power. It can also be used to make microelectronics, multiferroic solar cells, photovoltaic devices, and catalyzed water treatment systems. However, BFO's use in commercial devices is constrained by significant difficulties which results in degradation of its magnetoelectric response.

1.6.8 Critical BFO Issues

BFO is the only single-phase multiferroic material that has maximum spontaneous polarization at room temperature among all multiferroic materials. But the existence of various defects like oxygen vacancies and very high leakage currents prevents it from being used in commercial applications [60, 61]. Secondary phases occur such as $Bi_{25}FeO_{40}$, $Bi_2Fe_4O_9$, $Bi_{0.5}Fe_{0.5}O_{19.5}$, $Bi_{46}Fe_2O_9$, Bi_2O_3 and Fe_2O_3 are caused by the volatilization of bismuth this is the reason we use bismuth excess in precursors. BFO-based thin films are presently the focal point of study since they offer better leakage current and potential application for multifunctional gadgets [62, 63].

By altering processing parameters to reduce some of these issues and using appropriate deposition processes, high-quality thin films can be produced. The researchers discovered that BFO magneto-electric coupling can be improved through a variety of methods, including thin films, doping, and applying a high electric field [64].

The major disadvantages of this material that make it unsuitable for technical applications are as follows:

1.6.8.1 Difficulty in formation of single phase

Two basic factors are responsible for the production of impurity phases. Impurity phases are formed when bismuth evaporates during synthesis due to its relatively low breakdown temperature.

1.6.8.2 Electrical Resistivity

The valence state of iron changes from Fe^{+3} to Fe^{+2} when oxygen is scarce, resulting in charge defects during synthesis and a significant leakage current. As a result, ferroelectric properties of BFO decrease when the leakage current is significant.

1.6.8.3 Cycloidal Spin structure

G-type antiferromagnetic ordering is followed by $BiFeO_3$ [65, 66]. A canted AFM(antiferromagnetic) ordering of Fe^{+3} spins in bulk BFO produces the DM(Dzyaloshinskii-Moriya) interaction, resulting in a weaker ferromagnetic response. Spin cycloidal structure of BFO from ferromagnetism can't be recognized easily.

1.6.8.4 Weak Magneto-electric Coupling

The macroscopic magnetization cancel and limit the magnetoelectric coupling due to the spiral spin structure of BFO as indicated by Dzyaloshinskii-Moriya. So, it is very difficult to measure the weak magnetoelectric signal and is not very useful for the magneto-electric coupling devices. The expected thought of involving substrates in thin films with mismatched lattice parameter with BFO which create strain effects and potentially help in destruction of spiral spin structure is actually a valid approach in certain systems. BFO has a complex spiral spin structure known as a cycloidal structure, where the atomic spins forms the helical pattern [67]. First and foremost, Ramesh's gathering in 2003 effectively upgraded the multiferroic properties at room temperature in epitaxial BFO thin film heterostructure [47].

1.7 Motivation

Bismuth Ferrite is the only single-phase multiferroic material at room temperature. But the oxygen vacancies and strong leakage current are the defects that prevents it from being used in commercial devices [60, 61]. Also by the volatilization of bismuth secondary phases are produced in solid state synthesis. Due to the high annealing temperature these volatilization issues arises; because bismuth has low melting point it vaporizes from the material at high temperature and oxygen vacancies are left, which devalue its multiferroic properties by increasing the leakage current. So, the interesting optical and magnetoelectric properties are not completely achieved in bulk BFO. In this research we focus on chemically derived pure and doped BFO thin films. As there are plenty of BFO issues like high leakage current that should be discussed. In order to prepare chemically derived BFO thin films, the diol method has been used. This synthesis requires high temperature annealing in furnace. BFO has complex crystal structure, consisting of perovskite-like layers. High temperatures are often needed to promote the formation of the desired crystal structure and support the atoms to be arranged in the correct configuration. During the synthesis procedure some precursor materials may contain volatile species or impurities which

need to be removed. High temperatures are effective to obtain a purer BFO product. This is particularly important for achieving high quality BFO samples for various applications. Also, to achieve pure phase and to stabilize the Bi ion it should be replaced with suitable cation of low volatilization. For this, La^{+3} is doped at the A-site of BFO. La^{+3} has ionic radii of (1.16 Å) as compared to the ionic radius of Bi^{+3} (1.17 Å) so by adding La^{3+} exerts strain on the system and help in stabilization of the perovskite phase. Optical bandgap of the system with lower centrosymmetry is higher than the high centrosymmetric system which results to lower the bandgap of BFO which is very helpful in optoelectrical devices.

La^{+3} and Bi^{+3} both have same oxidation states and as BFO itself creates a net positive charge due to Bismuth(Bi) vacancies, so doping of La introduces additional positive charges. Also Fe^{+3} in the B-Site of BFO is replaced with trivalent ion i.e. Mn^{+3} cation which will help to suppress the oxygen vacancies, maintain the overall charge of the material and hence useful in reducing the leakage current. To study about the optimization of the synthesis procedure by the co-substitution of cations in order to attain the pure phase of BFO and to obtain the structural and optical properties of pure, doped and co-doped BFO thin films are the aim of present research. Monitoring the effect of dopants in the reduction of leakage current and behavior of leakage in multiferroic bismuth ferrite thin films are the main objectives of this work.

Chapter 2 Experimental Techniques

This chapter discusses the experimental research setups and methodologies that were used in this research work. This chapter includes the detailed description of pure, substituted and co-substituted BFO thin films. All experimental techniques and characterization used for this method for BFO thin films are shown in a flow chart given below:

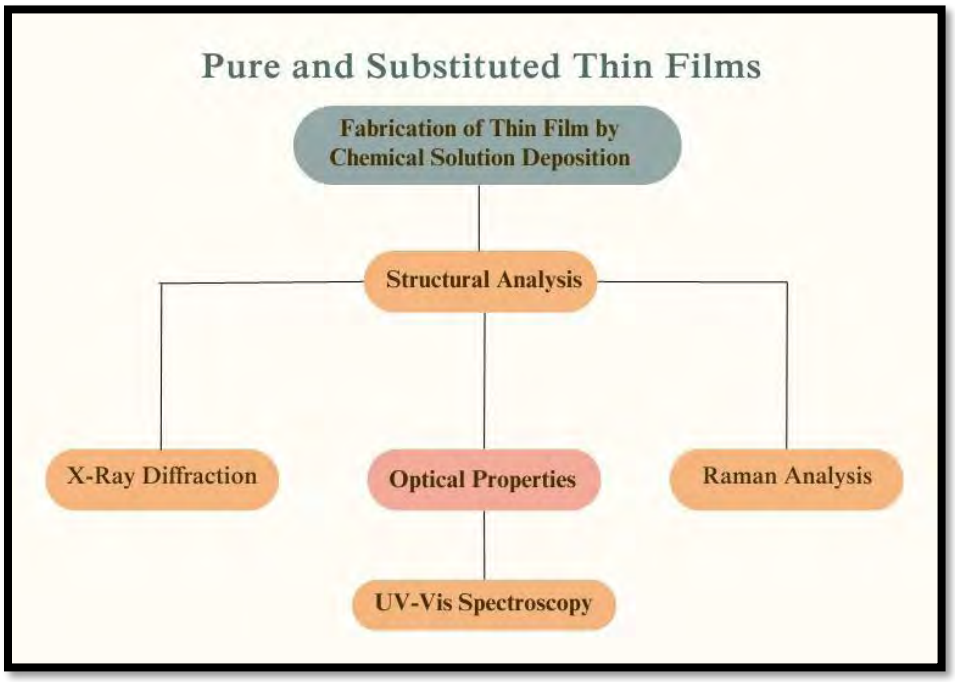

Figure 2.1: Flow chart of experimental techniques used.

2.1 Synthesis Equipment

2.1.1 Sonicator

In the fabrication of thin films, the first step is to clean the desired substrates properly on which thin films can be grown. For this purpose, sonicator is used. Sonicator is a laboratory instrument that is used for sonification process. It involves the application of sound waves or ultrasonic waves to a sample, typically placed in a liquid medium to disrupt cellular structures, to disperse particles, or to promote chemical reactions.

There are three stages for substrate cleaning.

2.1.1.1 Isopropanol

First and foremost, the substrates are cleaned in Isopropanol. Substrates are placed in a glass beaker having Isopropanol and plunged with the tip of the Sonicator. Sound waves with a recurrence scope of 20 kHz have been applied for 10 minutes.

2.1.1.2 Helimanex

From this point onward, the cycle is repeated by putting the substrates in helimanex. It produces bubbles in beaker which is the identification of substrates cleaning.

Figure 2.2: Sonicator used for substrates washing.

2.1.1.3 Deionized Water

Furthermore, the substrates are sonicated in deionized water for 10 minutes and this is our last step. These sound vibrations are useful in eliminating the toxins that are stuck with substrates. This cycle is known as ultra sonification.

2.1.2 Magnetic Stirrer and Hot Plate

When pure and substituted BFO thin films are synthesized, a magnetic stirrer and hot plate are used to ensure the homogeneous blending of the synthesized chemicals. It is a device which is used to generate the rotating magnetic field that is necessary to rotate the stirrer in the liquid. The stirring rate can be changed using the knob of the magnetic stirrer machine and can be set to meet the requirements of our experiment.

Figure 2.3: Magnetic Stirrer and hot plate.

The magnetic stirrer consists of a hot plate that is used to maintain the proper temperature during the synthesis process. It is also used for the initial heat treatment of the spin coated substrates at 250 ºC. A hot plate and magnetic stirrer is shown in the figure 2.3.

2.1.3 Tube Furnace

In tube furnace all the final substrates are annealed to reach the required phase for the pure and substituted BFO thin films. Temperatures up to 1000°C can be handled by this device. All of the prepared thin film samples are annealed at 600°C for 1 hour. The figure of the Tube furnace used for that purpose is shown in figure 2.4.

Figure 2.4: Tube Furnace.

2.1.4 Spin Coater

It is widely used to deposit thin films uniformly on a desired substrate. This procedure is used to deposit layers of various thicknesses on the desired substrate. It includes a sample placing area to hold film where we can stick our film using some adhesive material and a rotator that spreads the solution uniformly around the whole surface. Its rotation per second can be adjusted to meet the requirements of the project. The film's spinning speed can be used to regulate its thickness.

There are two ways for the precursor solution to be distributed on the surface of the substrates.

- **Static dispense** solution is dropped over a stationary substrate and covered the whole surface and spun at our required speed.
- **Dynamic dispense** solution is dropped on the center of the substrate and instantaneously the solution is pulled outward uniformly by the centrifugal force. The whole substrates surface is covered with the solution by centrifugal force and excess solution is flung off [68]

Figure 2.5: Spin Coater

2.1.5 Centrifugation

For this technique, molecules of various densities are separated using a centrifuge machine. They are put in a falcon tube and subjected to centrifugal force; the rate of centrifugation is determined by the angular velocity (usually expressed in revolutions per minute, or RPM), or acceleration (expressed in g-forces). The precipitates are separated and removed during centrifugation, leaving a clear solution in their place. This method is frequently employed to

examine the hydrodynamic properties of macromolecules and to separate solids from concentrated solutions.

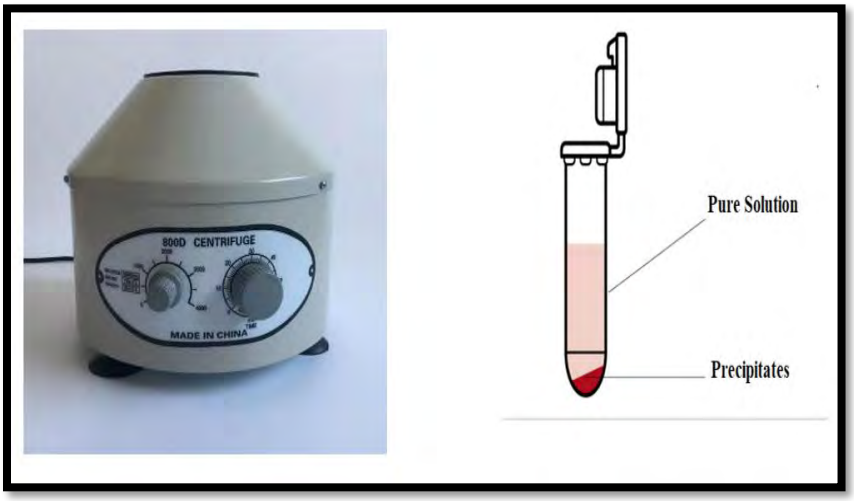

Figure 2.6: Centrifuge Machine and Falcon Tube.

2.2 Structural Analysis

Using an X-ray diffractometer and Raman spectroscopy, structural analysis of pure, La-doped, Mn doped and La-Mn co-doped BFO thin films was carried out.

2.2.1 X-Ray Diffractometer (XRD)

When a beam of X-rays interacts with the structure of a material then X-ray diffractometer is a measuring instrument for analyzing its scattering pattern.

2.2.1.1 X-Rays

X-rays are highly energetic electromagnetic radiations. Their energy ranges from 200 eV to 1 MeV. They are produced using external beam of electrons.

2.2.1.2 Production of X-rays

X-rays are produced inside an X-ray tube, which has two metal electrodes and is enclosed within a vacuum chamber. A tungsten filament cathode is heated to produce electrons. Electrons are pushed in the direction of the anode, which is maintained at ground potential, as the cathode is kept at a very high negative potential. These fast electrons fall with a water-cooled anode, losing energy upon impact with the metal anode, which is then transformed into X-rays.

2.2.1.3 Diffraction

Through their interaction with other objects, light or waves can change their behavior is called diffraction.

Figure 2.7: PAN analytical EMPYREAN X-ray Diffractometer.

2.2.1.4 Working Principle

Monochromatic X-rays and a crystalline sample interact constructively during X-ray diffraction. These X-rays are produced using a cathode ray tube made to create monochromatic radiation, which is then focused and directed at the sample using collimation. General scattering occurs when an incoming X-ray beam interacts with a crystal lattice. However, because of destructive interference, the majority of this dispersion cancels out. When scattering in a particular direction is in phase with dispersed rays from other atomic planes, diffraction takes place. These circumstances lead to the formation of new wavefronts, which through constructive interference reinforce one another and produce improved diffraction patterns.

So, Bragg's law or equation by which the diffraction occurs is given as

$$n\lambda = 2d\sin\theta$$

Here "λ" is the wavelength of X-rays and "d" is the crystal's interplanar spacing and "θ" is X-ray incidence angle.

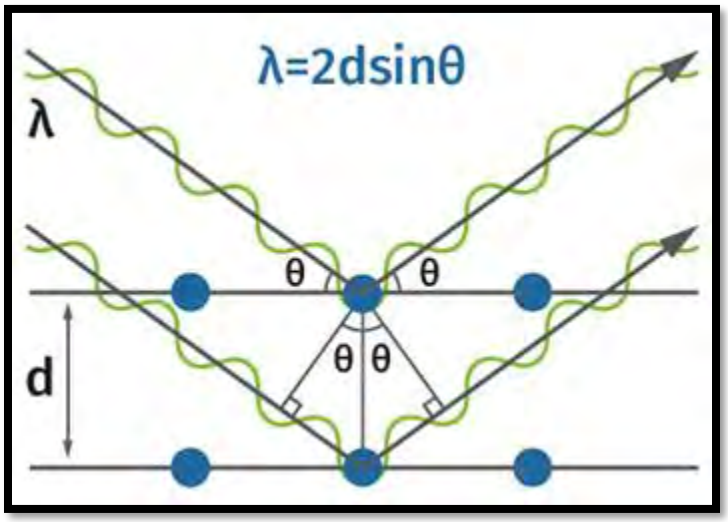

Figure 2.8: X-ray diffraction from lattice planes.

In X-ray beams if we consider two waves (Y and Z) fall on the surface of a crystal that is in phase. If from the first layer Y ray gets reflected i.e., the line AB and the Z ray gets reflected from the second layer of atoms i.e., the CD line, then it is obvious that ray Z has to travel a longer distance as compared to the ray Y and that distance is equal to QRS to emerge out of the crystal. If after reflection rays Y and Z are in phase and the two rays differ in distance travelled by two rays equals to an integral multiple of wavelength, then constructive interference occurs and satisfies Bragg's Law.

Every substance, whether crystalline or amorphous, has a specific atomic structure that, when subjected to X-ray diffraction, produces an identifiable trend. A fundamental equation that links the electromagnetic radiation's wavelength to the diffraction angle and the lattice spacing in a crystalline sample governs this phenomenon. The diffracted X-rays are then found, analyzed, and measured. Due to the random orientations of powdered materials, we must scan a wide range of "2" angles and investigate almost every known diffraction direction in order to identify the lattice structure. The identification of the mineral is possible by translating the diffraction peaks into the distinctive set of "d" spacings that each mineral displays. Each mineral has a set of distinct "d" spacing, so converting the diffraction peaks to "d" spacing enables identification of the

mineral. For the purpose of determining the crystal structure, a PANanalytical EMPYREAN system X-ray diffractometer with prefix optical modules and a fixed sample stage, operating at 40 kV and 35 mA, was employed for the measurement. (Cu-K, λ=1.5418) which is a monochromatic X-ray beam is allowed to fall on the sample and detector detected the intensity of the reflected beam. The sample, the counter and the X-ray source are all coplanar. This data for the "2θ" range lie between 20º to 60º with 0.02º increments and a 2 sec stay time. Bragg's Brentano geometry was employed for the XRD analysis. Fixed divergence slits are supplied with the instrument. It is necessary to insert these fixed divergence slits into the Prefix module's slots. There is an X-ray source, a sample stage, and a detector in a powder X-ray diffractometer as shown in figure 2.9.

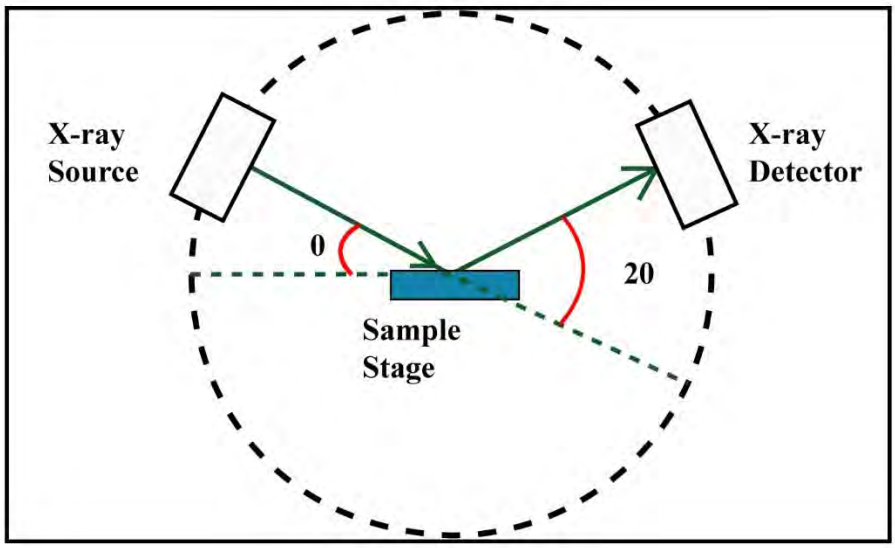

Figure 2.9: Powder X-ray Diffraction.

To study the powdered samples, a receiving slit of 1/16° and 1° fixed divergence slit is used in Bragg-Brentano geometry.

2.2.2 Raman Spectroscopy

Raman spectroscopy, which is used to look into a material's rotation, vibration, and low-frequency phonon modes, is regarded as the figure-print of the substance. A substance may reflect, absorb, or transmit when a monochromatic light probe is passed through it. Structural and chemical information about the molecule is provided by Raman spectroscopy basing scattering. The sample is radiated with a coherent laser source. Rayleigh scattering includes a phenomenon which occurs when light or other electromagnetic radiation interacts with particles or molecules that are smaller

than the wavelength of the radiation that falls. A small part that is made up of Stoke and anti-Stoke, is scattered inelastically. The inelastic anti-Stoke part provides us the information that is useful for our work. Monochromatic light knocked the molecule throughout the experiment from a lower to a higher energy level and then revived it to its initial state by releasing a photon with three different frequencies.

Rayleigh scattering $v_{Emitted\ Photons} = v_{Incident\ Radiation}$,

Stoke scattering $V_{Emitted\ Photons} < V_{Incident\ Radiation}$, and

Anti-Stoke scattering $V_{Emitted\ Photons} > V_{Incident\ Radiation}$.

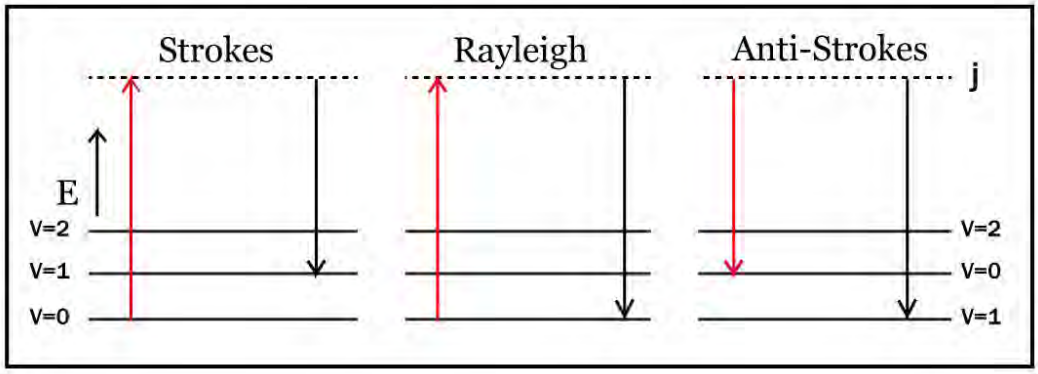

Figure 2.10: Raman scattering energy level diagram. The intensity of incoming light is shown by the red arrows in the interplay between matter and light. Black arrows indicate the stoke, anti-stoke, and Rayleigh scattered light intensity.

The majority of these frequencies are linked with changes in the rotation, vibration, and electronic state of the chemical system. Dispersed radiation frequently demonstrates polarization parameters that are different from those of the incident radiation. Scattering occurs in all directions; the direction of viewing has an influence on the radiation's strength and polarization. By examining the Raman spectrum, Raman spectroscopy can be used to extract structural data such as bond vibrations or the numerous modes resulting from structural distortions in the material.

By using a Laser Micro Raman spectrometer in present work Raman spectra of spin-coated thin films was attained at room temperature. The approach proved beneficial in determining the structural distortion in pure, doped, and co-doped BFO thin film samples.

2.2.2.1 Working Principle

In Raman Spectroscopy the incident light from the source is focused on the sample by using an objective lens and a monochromator. Raman scattering is frequently weak in comparison

to powerful Rayleigh scattering. To discriminating between in-elastically scattered light and intense Rayleigh scattered laser light is the most difficult problem while using Raman spectroscopy. Rayleigh scattered light is eliminated by the notch filter, and the remaining scattered light is transmitted to the spectrometer. The Raman spectrometer schematic diagram is shown in Figure 2.11. It is increasingly being carried out using charge-coupled devices (CCDs).

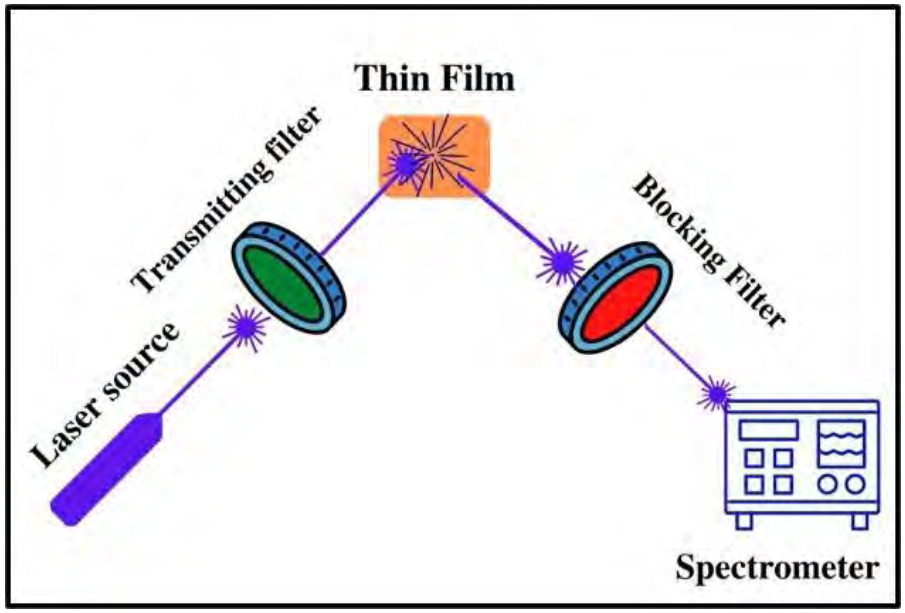

Figure 2.11: Schematic representation of Raman Spectroscopy.

2.3 Optical Measurement

For finding the spectral properties of various substances multiple approaches are available. For determining the wavelengths of optical spectra given as transmittance, reflectance, and absorption spectrometer is a widely used tool. The spectroradiometer is used to find out the spectral emission. We utilize a photo spectrometer for optical experiments because reflection spectra make it simple to identify the band gap and its variation.

2.3.1 UV-Vis Spectrometer

For measuring the optical properties, the device which we used is the “Lambda 950” double beam spectrometer which can operate in the ultraviolet, visible (UV/V's) spectral ranges. Also, the “Lambda 950” operates near the infrared region. A twofold beam is present in the spectrometer, double monochromatic and all reflecting optical system. All the optical parts are silica-coated for sturdiness. Typical features of the lambda 950 spectrometer features are shown in the figure 2.12.

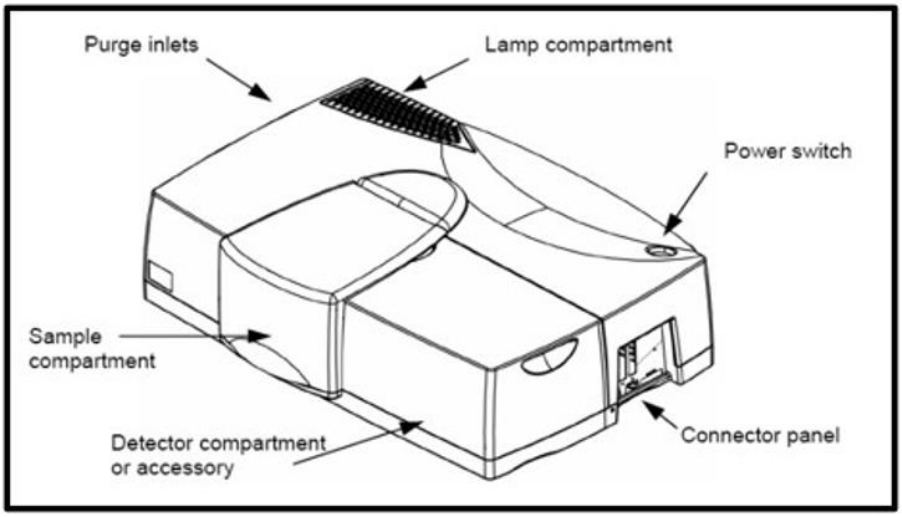

Figure 2.12: UV-Vis Spectrometer Lambda 950.

It is given with the four windows and the spectrometer's entire container is completely sealed. Similarly, by using windows a barrier that is sealed, separates the sample compartment from the optical compartment and detector component. Silica made windows can be used throughout the full spectrum range given. Sample compartment is completely sealed by windows in order to protect the optical instruments from dust and seething.

Lambda 950 spectrometer includes two sources of light.

- One is the deuterium lamp (DL) which is able to operate in the UV region.
- And the next is the halogen lamp (HL) which functions in the visible and near infrared (NIR) region. It covers the entire range of spectrometers that is from 175nm-3300nm.The spectrometer can scan from maximum to minimum wavelengths. There are four windows in the spectrometer. All optical compartments of the spectrometer are sealed. Also, the sample compartment is sealed using a window between the detector component and the optical compartment. The silica windows that seal the sample chamber protect the instrument's optical parts from gases and dust.

Chapter 3 Synthesis and Structural Characterization

In this chapter optimization of the synthesis procedure and structural analysis of pure and substituted thin films of BFO are discussed in detail.

3.1 Synthesis Techniques

For the fabrication of pure and substituted BFO thin films, various techniques have been extensively used such as chemical solution deposition, Pulsed laser deposition (PLD), Laser chemical vapor deposition and RF-magnetron. However, in present study Chemical Solution Deposition technique is used to fabricate BFO thin films because this is the most efficient and cost-effective method for thin film deposition.

3.1.1 Chemical Solution Deposition Technique

For the fabrication of thin films, chemical solution deposition (CSD) technique was used. In this method, the precursor solutions was being synthesized and then spin-coated to fabricate thin films. This method is also known as sol-gel processing. The precursor chemicals of the required material in CSD are dissolved into the solvents, then refluxed and at last it is centrifuged. Prepared solution was then deposited on the glass substrates and annealed at specific temperature to get the required material. It is commonly used in the preparation of Perovskite materials for manufacturing as well as ceramics, glasses, composites, and Perovskites. It is a low-cost thin film production method that has a large surface area and good uniformity. PLD and sputtering need refined methods including vacuum processing and specialized tools. However, the CSD deposition process can be carried out in the atmosphere circumstances at room temperature [12].

3.1.2 Thin films fabrication by CSD Technique

This method serves as an initial point for the fabrication process. A metal compound (alkoxides, metal chlorides, or metal nitrate) is combined with solvent and metal complexing agent in a specific precursor. To prepare $BiFeO_3$, intially two separate solutions were prepared i.e., one is for bismuth nitrate and one is for iron nitrate. Bismuth nitrate and iron nitrate are present in stoichiometric proportions were taken in a beaker to prepare 0.5 M solution and calculated amount of N-methyldiethanolamine(MDEA) and 1,3 propane diol were added which function as a solvent. Both solutions were in a state of stirring for 48 hours at room temperature. After that refluxing

(stirring + heating) was done for 1 h at 250°C and 5 minutes at 290°C. When the heating process was completed, at this stage ethanol was added to both the solutions to recover their initial quantity of the solutions, if some solution was lost during heating process. Again both the solutions were stirred for 30 minutes after the addition of ethanol. After stirring, final solution was prepared by adjusting the molarity of the solution to be equal to 0.1 M. For this purpose, further ethanol was added to dilute the solution and make it equal to 0.1 M. 2-3 drops of acetic acid was also added to the solution and stir again for 30 minutes. Prepared solution was centrifuged, filtered and ready to be used to fluorine-doped tin oxide (FTO) substrates for spin coating.

3.1.3 Precursors

Chemical solution deposition technique was used to fabricate thin films of pure and doped BFO in the present study. For this purpose, non-aqueous procedure was used in which Ethanol and acetic acid are utilized as organic solvents. Stoichiometric amount of precursors was used to prepare the BFO precursor solution. Chemical precursors used in the preparation of BFO precursor solution are shown in table 3.1.

Table 3.1: Chemicals used for thin film fabrication of pure and doped BFO.

Chemicals	Formula	Purity%	Suppliers	Mol. Weight (mol/g)
Bismuth Nitrate Pentahydrate	$Bi(NO_3)_3.5H_2O$	99%	Macklin	485.07
Iron Nitrate Nonahydrate	$Fe(NO_3)_3.9H_2O$	98.50%	Macklin	404
Acetic Acid	CH_3COOH	99.80%	Chem-lab NV	60.05
Ethanol(Absolute)(Ethyl Alcohol)	CH_3CH_2OH	99.80%	Lab-Scan	46.07
1,3 Propane diol	$C3H_8O_2$	98%	Macklin	76.09
MDEA(N-Methyl diethanolamine	$C5H_{13}O_2N$	≥99%	Aldrich	119.163
Lanthanum nitrate hexahydrate	$La(NO_3)_3 .6H_2O$	99.90%	Aladdin	433.01
Manganese nitrate tetrahydrate	$Mn(NO_3)_2.4H_2O$	99.90%	Emsure	251.01

3.1.4 Chemical Reactions

The chemical reactions for the preparation of samples are given below.

1. $BiFeO_3$ (BFO)

Pure BFO was prepared by using following chemical equation:

$$Bi(NO3)_3.\ 5H_2O + Fe(NO3)_3.\ 9H_2O \rightarrow BiFeO_3 \quad (3.1)$$

Following quantity of precursors were used for the preparation of pure BFO as shown in table 3.2.

Table 3.2: Concentration and calculated mass of different chemicals used for the preparation of BFO compositions.

x =0			y =0		
$Bi(NO_3)_3.5H_2O$	MDEA	Diol	$Fe(NO_3)_3.9H_2O$	MDEA	Diol
3.1528g	3.8728g	4.946g	2.5246g	3.724g	4.756g

Thin films of BFO with substitutions and co-substitutions were also prepared for this experiment.

2. $Bi_{1-x}La_xFeO_3$ (BLFO)

Balanced chemical equation used for the synthesis of La^{+3} substituted BFO sample is written below:

$$(1-x)Bi(NO3)_3.\ 5H_2O + Fe(NO3)_3.\ 9H_2O + xLa(NO3)_3.\ 6H_2O \rightarrow Bi_{(1-x)}La_x\ FeO_3 \quad (3.2)$$

Where x = 0.05, in order to reduce the presence of oxygen vacancies within the system, an extra 4% of bismuth nitrate was added. Mass calculated for different chemical precursors to prepare 0.1 M molar solution is shown in table 3.3.

Table 3.3: Concentration and calculated mass of different chemicals used for the preparation of La substituted BFO composition.

x = 0.05				y = 0		
$(1-x)Bi(NO_3)_3.5H_2O$	$x\,La(NO_3)_3.6H_2O$	MDEA	Diol	$Fe(NO_3)_3.9H_2O$	MDEA	Diol
2.9951g	0.1351g	3.856g	4.9351g	2.5247g	3.7178g	4.7556g

3. $BiFe_{(1-y)}Mn_yO_3$ (BFMO)

Balanced chemical equation used for the synthesis of Mn substituted BFO sample is shown below:

$$Bi(NO3)_3.\ 5H_2O + (1-y)Fe(NO3)_3.\ 9H_2O + yMn(NO3)_3.4H_2O \rightarrow BiFe_{(1-y)}Mn_y\ FeO_3 \quad (3.3)$$

Table 3.4: Concentration and calculated mass of different chemicals used for the preparation of Mn substituted BFO composition.

$x = 0$			y =0.025			
$(Bi(NO_3)_3.5H_2O$	MDEA	Diol	$(1-y)Fe(NO_3)_3.9H_2O$	$y\,Mn(NO_3)_2$	MDEA	Diol
3.0315g	3.7238g	4.7556g	2.4616g	0.0279g	3.7274g	4.7602g

4. $Bi_{1-x}La_xFe_{1-y}Mn_yO_3$ (BLFMO)

Balanced chemical equation used for the synthesis of La (substituted at Bi-site) and Mn (substituted at Fe-site of BFO) co-doped composition is shown below:

$$(1-x)Bi(NO3)_3.\ 5H_2O + (1-y)Fe(NO3)_3.\ 9H_2O + yMn(NO3)_3.4H_2O \rightarrow BiFe_{(1-y)}Mn_y\ FeO_3 \quad (3.4)$$

Where x = 0.05 and y = 0.025. 4% excess bismuth nitrate was also added in this sample. Quantity of different chemical precursors used for preparation of 0.1 M molar solutions, is shown in table 3.5.

Table 3.5: Concentration and Molecular weight of various chemicals used for the preparation of La and Mn co-substituted BFO compositions.

$x = 0.05$				$y = 0.025$			
$(1-x)$ Bi(NO3)3.5H2O	$x\,La(NO_3)_3.6H2O$	MDEA	Diol	$(1-y)$Fe(NO3)3.9H2O	$y\,Mn(NO_3)_2$	MDEA	Diol
2.9951g	0.1351g	3.8561g	4.9351g	2.4618g	0.0278g	3.7208g	4.7518g

3.2 Preparation of BFO Thin film

Bismuth nitrate ($Bi(NO_3)_3.5H_2O$), Iron nitrate ($Fe(NO_3)_3.9H_2O$ are the initial materials providing the source of Bi and Fe in the solution. Pure BFO solution is produced using a solution of iron and bismuth nitrate and by dissolving them in the solvent and metal complexing agent that was 1,3 Propane diol and N-methyldiethanolamine (mdea) by keeping the molarity of the solution to be equal to 0.5M. To make up for the bismuth eliminated during volatilization, 4% more bismuth nitrate was added. Firstly, Bi(III) solution was made by adding bismuth nitrate in a solution of

Diol and MDEA, using molar ratios of Bi(III):MDEA:Diol = 1:5:10 and same process was repeated for Fe(III) solution using same molar ratio. Both of the solutions were prepared separately in two flasks. For forty-eight hours, the solutions were stirred constantly at room temperature. After this both solutions were refluxed for 1 h at 250°C and then the temperature is raised to 290°C for 5 minutes. Now place them for half an hour so that their temperature becomes normal. Bi(III):Fe(III) = 1.04:1.00 was used to combine the two solutions of Bi(III) and Fe(III), which produced a BFO precursor solution with a 4% excess of Bi. Small drops of Acetic acid were used as solvent in order to increase the rate of hydrolysis thus stabilizing all solutions. Ethanol amine (ethanol) was also added in all solutions to retain the original quantity of the solution. Finally, 0.5M of solution's concentration was adjusted using ethanol and acetic acid. This BFO precursor solution was centrifuged and filtered at the end in order to remove precipitates. Now this solution can be used for spin coating on FTO substrates to form the desired films. Flow chart for BFO preparation is shown in figure 3.1 and figure 3.2 below:

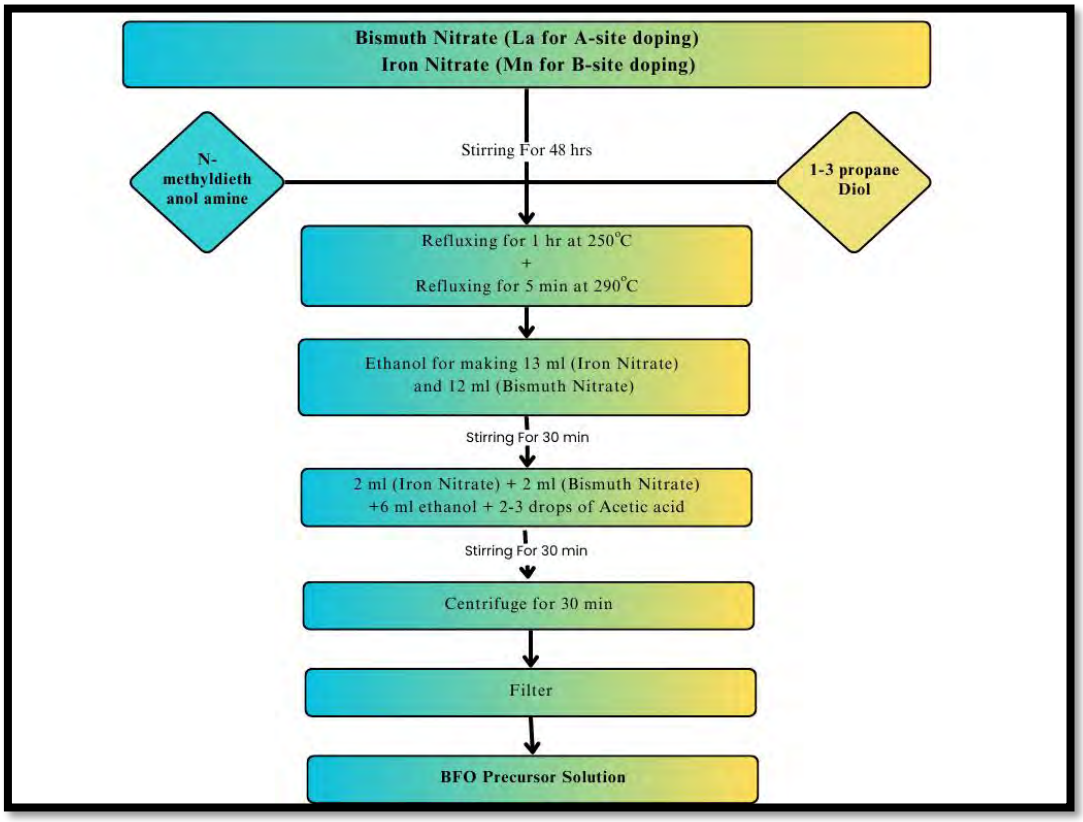

Figure 3.1: Flow chart of procedure formation of BFO pure and co-doped precursor solution by using Diol Method.

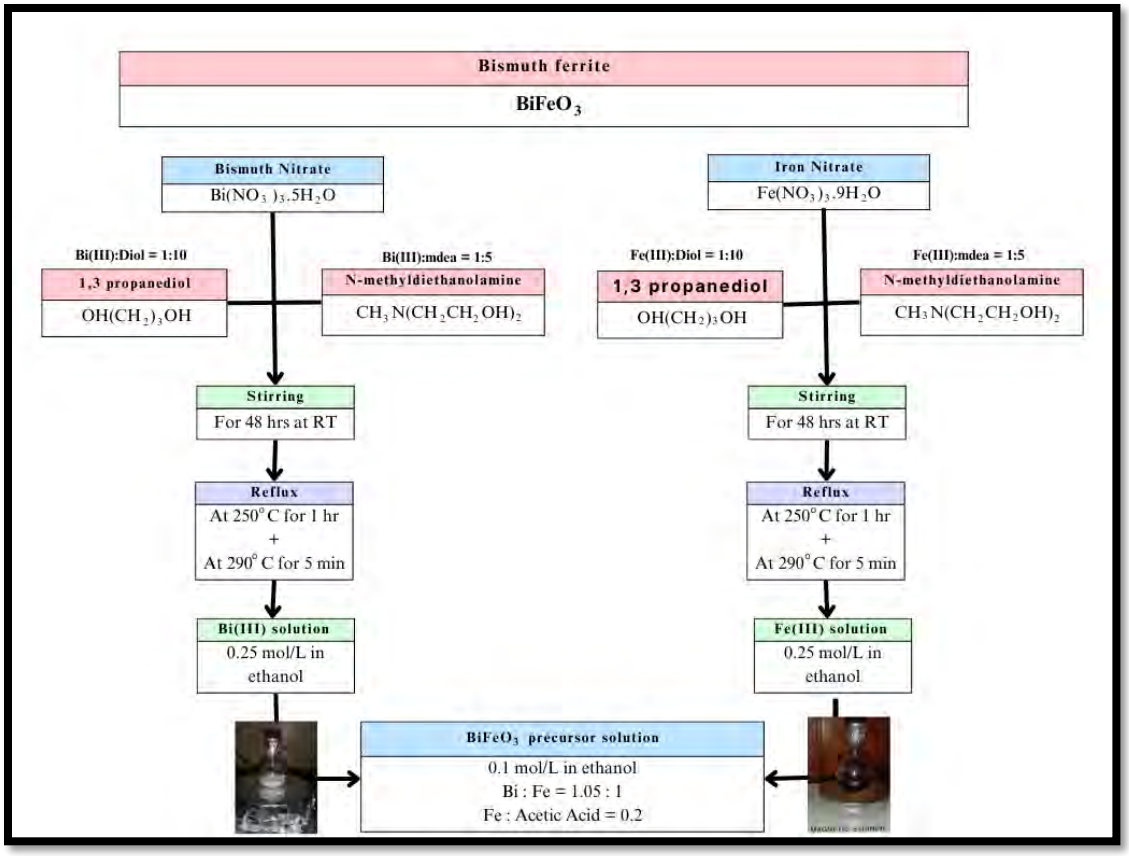

Figure 3.2: Flow chart of synthesis procedure used to prepare $BiFeO_3$ precursor solution.

3.2.1 Substrate Washing

The preparation of the FTO substrates was done before spin coating, they were cleaned using Sonicator. The substrates are cleaned in isopropanol for 10 minutes in the first stage in a beaker. Then, washed in Hellmanex solution for ten minutes. Finally, the substrates are cleaned for ten minutes in deionized water using sonicator.

3.2.2 Deposition technique using Spin coating

For depositing thin films on a substrate, spin coater was used. Detailed explanation of the spin coater was included in Chapter 2. It was used to prepare thin films of pure, La substituted, Mn substituted and La-Mn co-substituted BFO thin films on glass surfaces covered in fluorine-doped tin oxide (FTO) coating. 10-20 μl solution of either pure or doped BFO was poured onto the substrate in the spin coater and spun for 45 seconds at 2000 rpm (revolutions per second). To dry the coated layer, the sample was subjected for one minute drying period dried at a temperature of 150°C and then heated at 250°C on a pre-heated hot plate for 5 minutes. After that the film was

annealed at 600°C in a tube furnace for ten minutes. Place it for 2 minutes to cool down. In order to get the appropriate film thickness, this procedure was repeated eight times.

3.2.3 Heat treatment

After depositing the prepared solution on the substrate using spin coater, obtained film was finally annealed in a tube furnace for 10 minutes at 600°C. Figure 3.3 shows the entire fabrication process for pure BFO thin film.

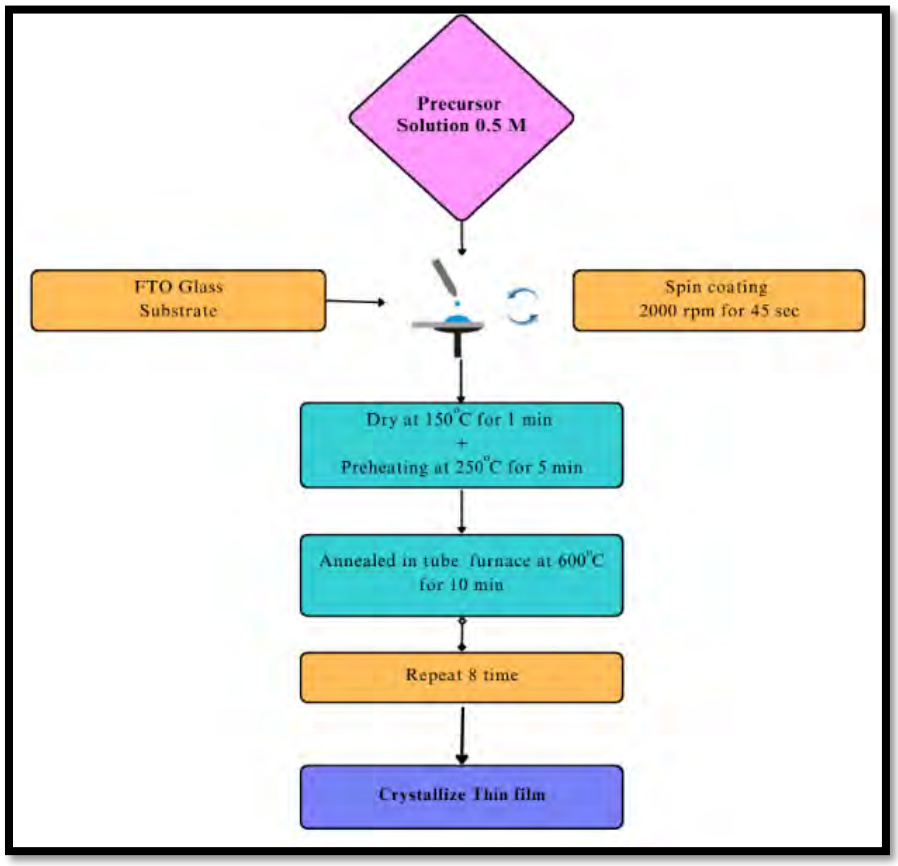

Figure 3.3: Production of thin film by spin coating method.

3.2.4 Synthesis of La substituted BFO thin film:

For the synthesis of La substituted BFO composition, stochiometric amount of Lanthanum nitrate hexahydrate ($La(NO_3)_3.6H_2O$) was also added along with the Bi nitrate solution. While the remaining procedure remains the same. The flowchart explaining the synthesis process can be seen in Figure 3.4.

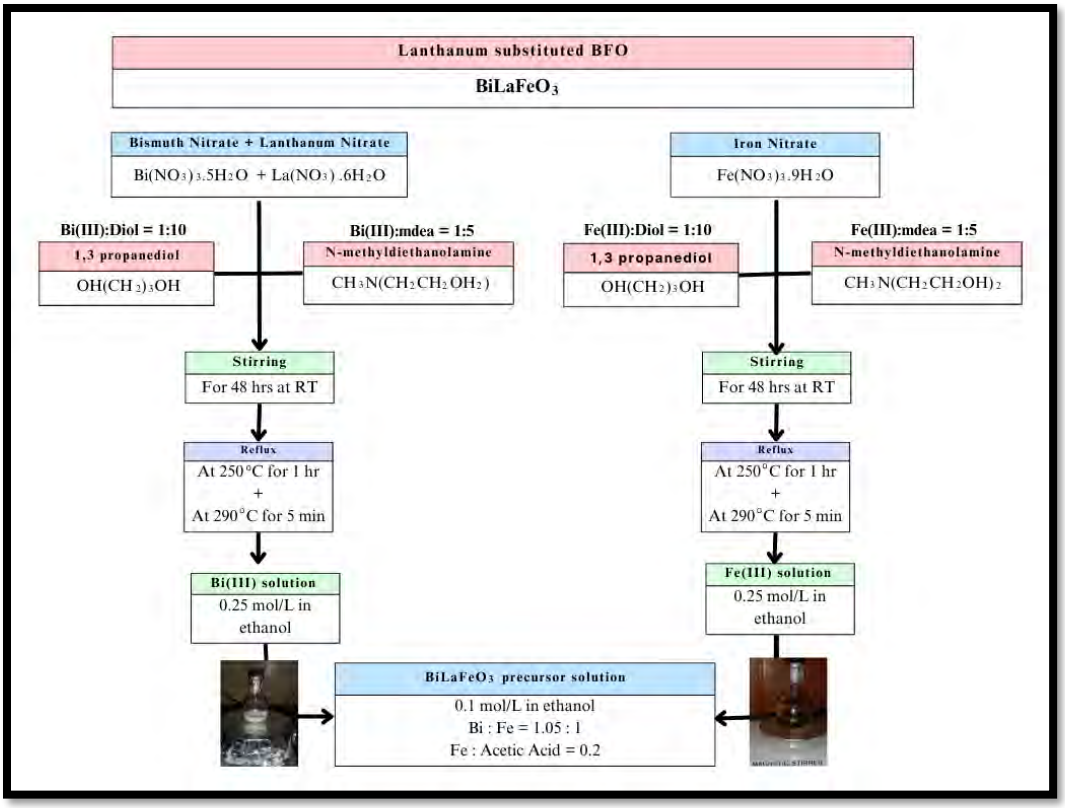

Figure 3.4: Flow chart of synthesis procedure used to prepare $Bi_{0.95}La_{0.05}FeO_3$ precursor solution-

3.2.5 Synthesis of Mn substituted BFO thin film

For the synthesis of Mn substituted BFO composition, stochiometric amount of Manganese nitrate tetrahydrate $Mn(NO_3)_2.4H_2O$ was also added along with the Fe nitrate solution. While the remaining procedure remains the same. Flow chart of the synthesis procedure is shown in figure 3.5.

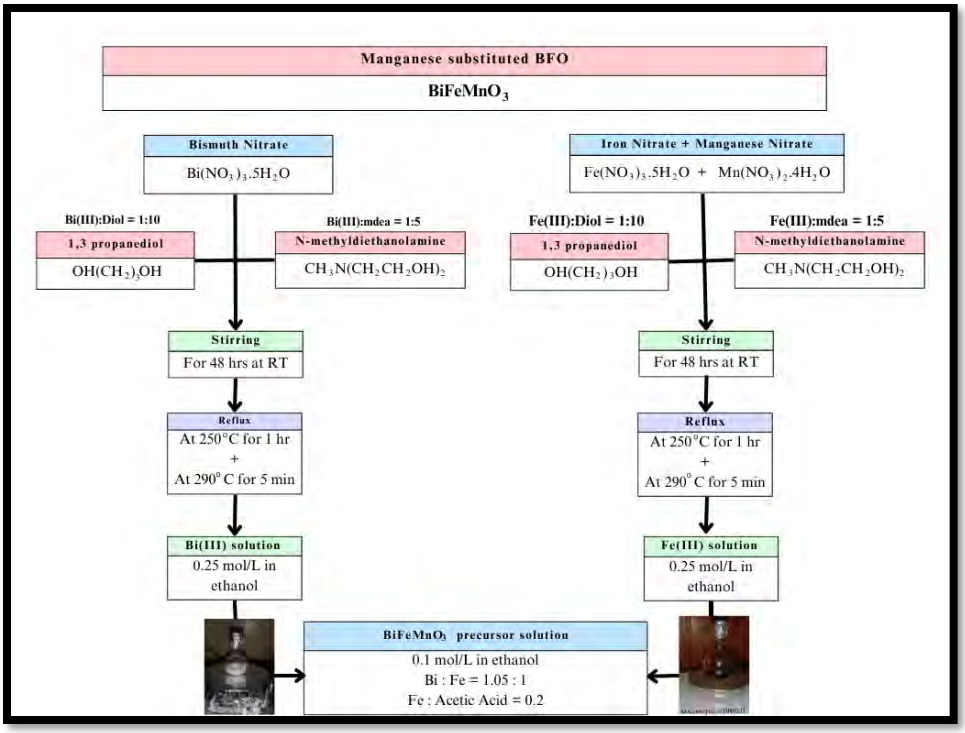

Figure 3.5: Flow chart of synthesis procedure used to prepare $BiFe_{0.975}Mn_{0.025}O_3$ precursor solution-

3.2.6 Synthesis of La/Mn co-substituted BFO thin film

For the synthesis of co-substituted BFO sample, stochiometric amount of Lanthanum nitrate hexahydrate $La(NO_3)_3.6H_2O$ was added along with the Bi nitrate solution and stochiometric amount of Manganese nitrate tetrahydrate $Mn(NO_3)_2.4H_2O$ was added to Fe nitrate solution. While the remaining procedure remains the same. Flow chart of the synthesis procedure is shown in figure 3.6.

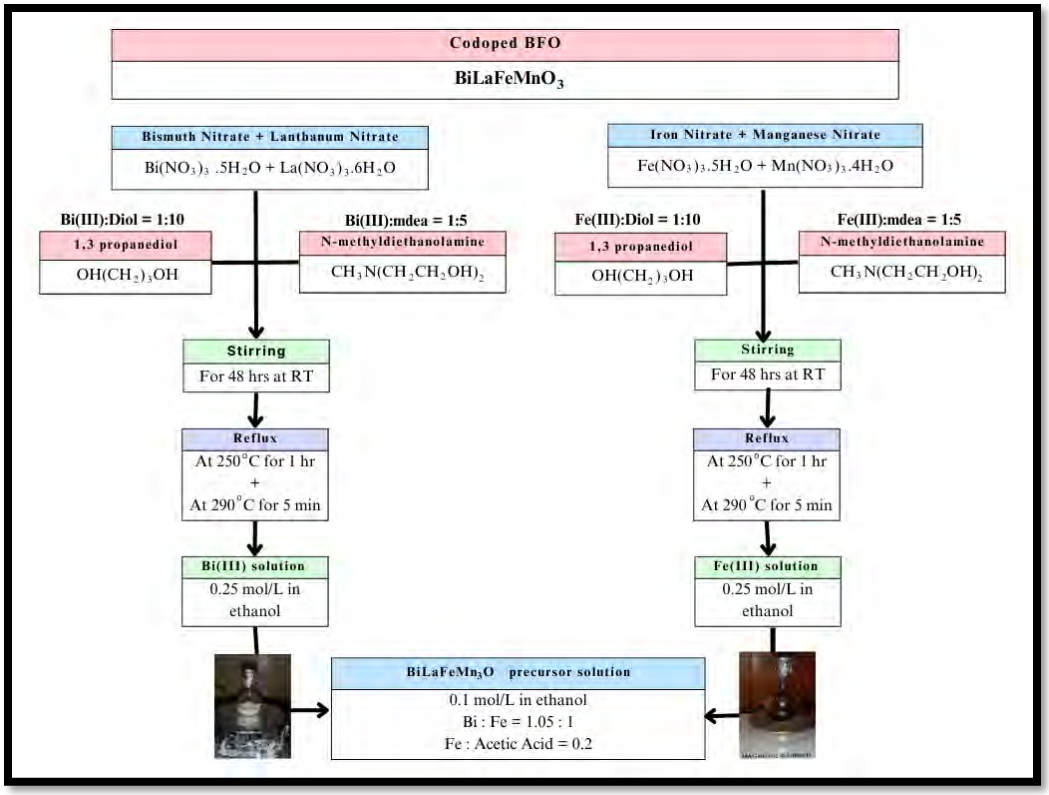

Figure 3.6: Flow chart of synthesis procedure used to prepare $Bi_{0.95}La_{0.05}Fe_{0.975}Mn_{0.025}O_3$ precursor solution-

3.3 Structural Analysis

3.3.1 XRD Diffraction

The structural investigation of thin films of BFO was carried out using the Empyrean PANalytical X-ray Diffractometer using Cu-K radiation with a wavelength of $\lambda = 0.154$ nm, both in its pure state and when substituted or co-substituted. X-ray Diffraction (XRD) spectrum of all four samples $BiFeO_3$, $Bi_{0.95}La_{0.05}FeO_3$, $BiFe_{0.975}Mn_{0.025}O_3$, and $Bi_{0.95}La_{0.05}Fe_{0.975}Mn_{0.025}O_3$, are shown in figure 3.7. There is no evidence of any type of secondary phases observed in all the compositions. From graph, it is observed that pure BFO thin film exhibit distorted rhombohedral structure (see figure 3.7 a and b) with space group R3c. High intensity peaks of rhombohedral structure are well separated from each other (deconvoluted peaks of BFO rhombohedral structure is shown in figure 3.8 (a)) and observed at ($2\theta = 31.81°$ and $2\theta = 32.11°$) with corresponding (104) and (110) planes respectively. This arrangement matched well with the standard card (ICDD 00-082-1254).

La^{+3} (x = 0.05) substituted BFO sample also exhibits rhombohedral structure. The main intensity peaks in La substituted BFO composition start to merge but structure still remain rhombohedral with no evidence of any type of structural transformation. To confirm the presence of rhombohedral structure, deconvoluted XRD peaks are shown in figure 3.8(b). Results of deconvolution also indicate the presence of rhombohedral structure. For comparison zoomed view of the XRD peaks of all the samples between angle 30° to 34° are shown in figure 3.8. XRD peak positions shift towards higher angle in $Bi_{0.95}La_{0.05}FeO_3$ sample, when compared with pure BFO sample. According to Bragg's law Inter-planar distance d is related to diffraction angle θ by following relation:

$$sin\theta \propto \frac{1}{d} \tag{3.5}$$

From above relation it is observed that when d decreases θ increases. Hence, decrease in d-spacing and lattice parameters results in shifting of the peak towards higher angle. As ionic radii of La^{3+} (1.16 Å) is smaller than Bi^{3+} (1.17 Å), so substitution of smaller ion of La^{3+} in place of Bi^{3+} results in decrease in d-spacing and volume with resultant shift in the peak towards higher angle.

XRD spectrum of $BiFe_{0.975}Mn_{0.025}O_3$ also indicates the evidence of rhombohedral structure with main intensity peaks appear to merge without any structural transformation (see figure 3.7 and 3.8). There is no evidence of shift in XRD peak observed in Mn substituted BFO sample when compared with the pure sample. As ionic radii of Mn^{+3} (0.64 Å) is quite similar with the ionic radii of Fe^{+3} (0.645 Å) so there is no change in volume and hence no peak shifting is observed in Mn substituted BFO sample. In La and Mn co-substituted composition, rhombohedral phase is observed with peak shifting towards higher angle. Due to size mismatch, La and Mn both cause strain in the system, shifting the peak towards greater angles.

In co-substituted $Bi_{0.95}La_{0.05}Fe_{0.975}Mn_{0.025}O_3$ sample, results of deconvolution indicate the presence of mixed rhombohedral and orthorhombic phase. As both the dopants have a ionic radii mismatch with the host ion so, both exert strain on the system and trigger the structure phase transformation towards cubic phase. Hence, mixed phase of rhombohedral and cubic structure is observed as shown in figure 3.8(d).

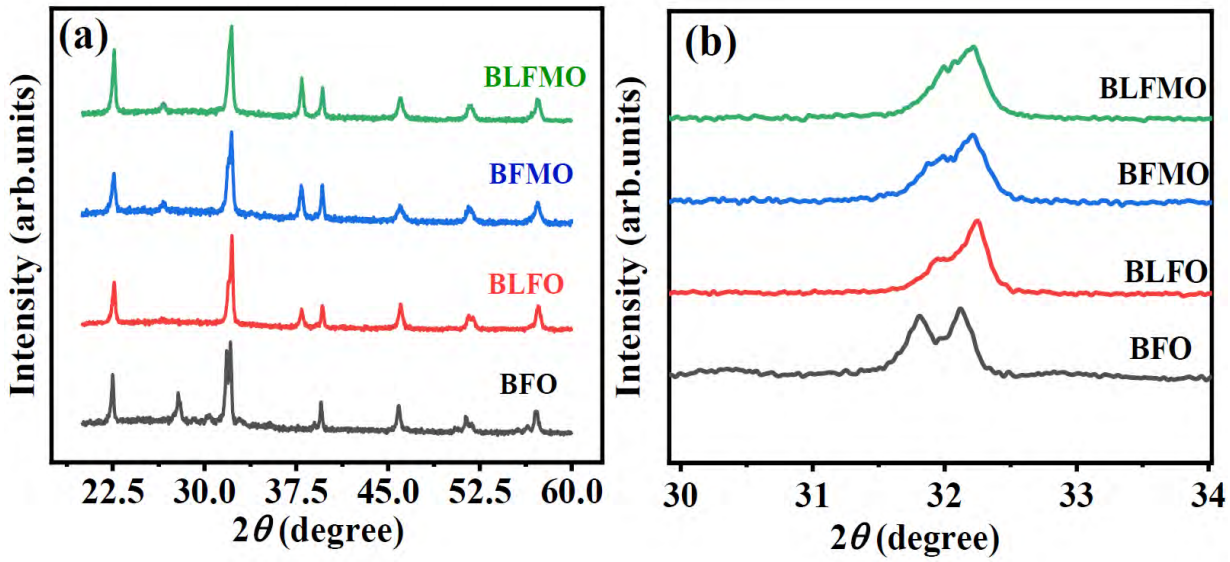

Figure 3.7: (a) XRD patterns of pure and doped $BiFeO_3$ thin films (b) Zoomed XRD of all samples.

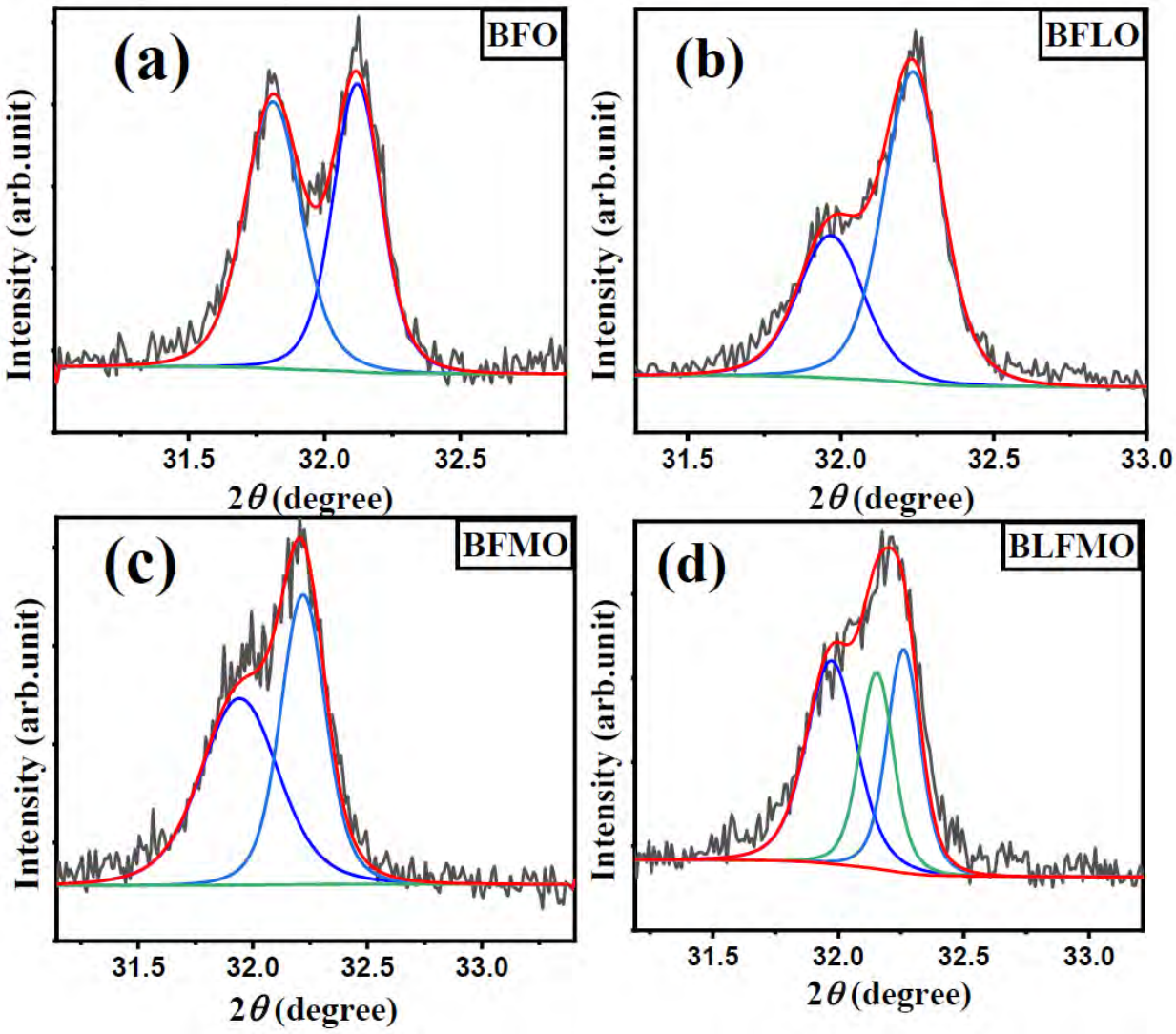

Figure 3.8: The Deconvolution Analysis of XRD Peaks (a) Pure BFO (b) La substituted BFO(c) Mn substituted BFO (d) Co-substituted BFO.

3.3.2 Calculation of Lattice Parameter

3.3.2.1 Rhombohedral Phase

The following relation is used to calculate the lattice parameters of pure and substituted BFO thin films for rhombohedral structures:

$$\frac{1}{{d_{hkl}}^2} = \frac{4}{3}\left[\frac{h^2 + hk + k^2}{a^2}\right] + \frac{l^2}{c^2} \tag{3.6}$$

Here d represents the inter-planar spacing distance between adjacent planes where the miller indices are h, k and l while the lattice parameters are a and c.

We can calculate the volume of all the compositions from the relation given as:

$$V = \frac{\sqrt{3}a^2c}{2} \tag{3.7}$$

Lattice parameters and volume of BFO thin films (pure and substituted) for rhombohedral structure are calculated and shown in table 3.6.

Table 3.6: Lattice parameters and volume of pure and La^{+3} doped BFO thin films samples.

$Bi_{1-x}La_xFe_{1-y}Mn_yO_3$	a_r (Å)	c_r (Å)	c/a	$Vol.$ (Å^3)
$x = 0, y = 0$	5.573	13.8492	2.484	372.586
$x = 0.05, y = 0$	5.552	13.7922	2.484	368.208
$x = 0, y = 0.025$	5.578	13.844	2.481	372.689
$x = 0.05, y = 0.025$	5.555	13.736	2.472	367.15

From table, it is observed that with addition of La^{+3} the unit cell volume and lattice parameter decreases.

3.3.2.2 Cubic Phase

The calculated lattice parameters of cubic phase of $Bi_{1-x}La_xFe_{1-y}Mn_yO_3$ are calculated by the following relation:

$$\frac{1}{{d_{hkl}}^2} = \frac{h^2+k^2+l^2}{a^2} \tag{3.8}$$

Where h, k and l are the miller indices. a, b and c indicate the lattice parameters and d is the inter-planner spacing.

Volume of samples can be calculated by using the formula:

$$V = a^3 \tag{3.9}$$

Calculated lattice parameters and volume of sample are shown in table 3.7.

Table 3.7: Lattice parameter of cubic phase.

$Bi_{1-x}La_xFe_{1-y}Mn_yO_3$	a_c (Å)	$Vol.$ (Å^3)
$x = 0.05, y = 0.025$	4.7995	110.5574

3.3.3 Raman Analysis

At room temperature the Raman spectra of the pure, substituted, and co-substituted samples are taken in order to perceive the structural phase change triggered by La^{+3} and Mn^{+3} doped and La^{+3}-Mn^{+3} co-doped substitution in BFO.

3.3.3.1 $BiFeO_3$

At room temperature the Raman spectra of the pure, substituted, and co-substituted samples are taken to find out the structural phase transition triggered by substitution of dopant. In figure 3.9 Raman spectra of pure BFO sample are shown. For a rhombohedral (R3c) structure, 13 Raman active modes are predicted by group theory, four of which are A1 and nine of them are E modes i.e., Γ_{Raman} = 4A1+9E [69]. In a $BiFeO_3$ perovskite structure, modes observed in the lower frequency region corresponds to the bismuth ion vibration in the structure. While modes observed in the higher frequency region are related with the vibration of Fe-O octahedral structure. E1, E2, and A-1 modes in pure BFO are observed at 110 cm^{-1}, 122 cm^{-1}, 161 cm^{-1}, that agrees with the results of Yu-Jie Wu et.al [70]. Deconvolution of Raman modes are also done to identify the presence of different modes as shown in figure 3.15.

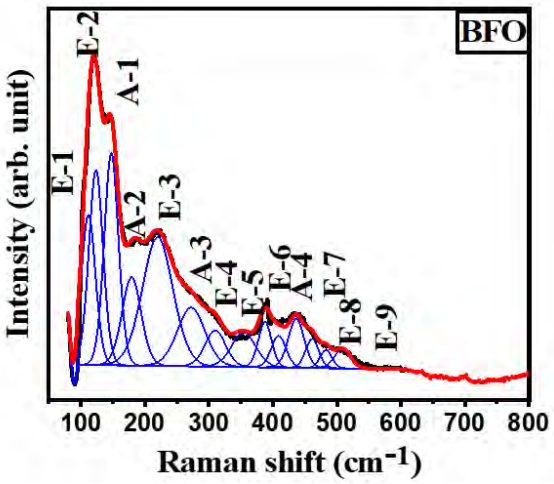

Figure 3.9: Raman spectra of Pure BFO thin films at room temperature.

3.3.3.2 $Bi_{1-x}La_xFeO_3$

To find out the structural changes triggered by La^{+3} substitution, the observed Raman modes are compared with the Raman modes of pure BFO. In figure 3.10 Raman spectrum of $Bi_{0.095}La_{0.05}FeO_3$ are shown. The Raman modes of La^{+3} (x = 0.05) substituted BFO are seen to match quite well with the Raman modes of pure BFO, which indicate no structural change and the modes dominantly correlate to the rhombohedral phase [71]. This result agrees with the XRD analysis which also indicates no evidence of any structural phase transition. In La^{+3} (x =0.05) substituted BFO composition, the peak corresponding to A1 mode is located at 161.47cm^{-1} in pure BFO and shifts to 171.06 cm^{-1} with a 5% substitution of La^{+3} in place of Bi^{+3}. As shown by the red arrow in figure 3.12. As Bi-O bond vibrations corresponds to lower frequency modes so, substitution of La^{+3} affects the Bi-O bond vibrations, thus altering their mode intensities. It is found that BLFO showed the same BFO modes, but slight decrease in intensity of the modes accompanied by shifting to a higher frequency. These displacements specify that the lanthanum atom is substituted in place of bismuth in BFO A-site.

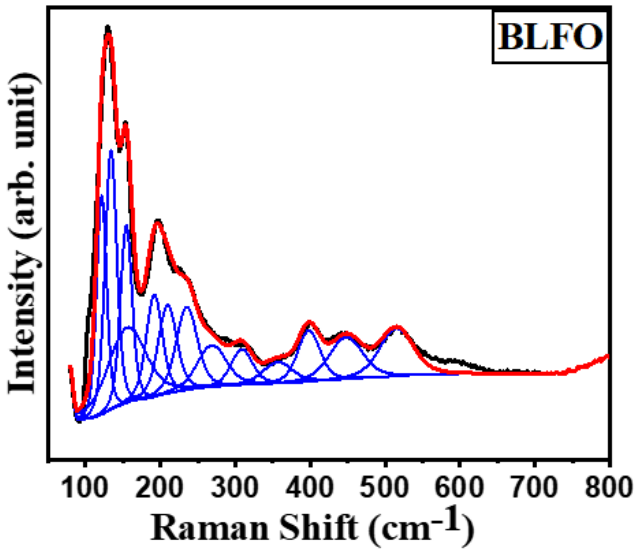

Figure 3.10: Raman spectra of La^{+3} substituted BFO thin films.

3.3.3.3 $BiFe_{1-y}Mn_yO_3$

Raman spectrum of Mn substituted BFO composition is shown in figure 3.11. It is observed from the graph that substituting Mn^{+3} (y = 0.025) at B-site of BFO, modes of E1, E2 and and become wider and intensities of these modes increases by adding dopant and they overlap with A1 mode but structure still remains rhombohedral. No evidence of any new mode is observed. Raman

spectra of $BiFe_{1-y}Mn_yO_3$ is shown in figure 3:11. Result of Raman analysis of Mn substituted BFO composition is consistent with XRD analysis which also indicates no evidence of structural phase transformation.

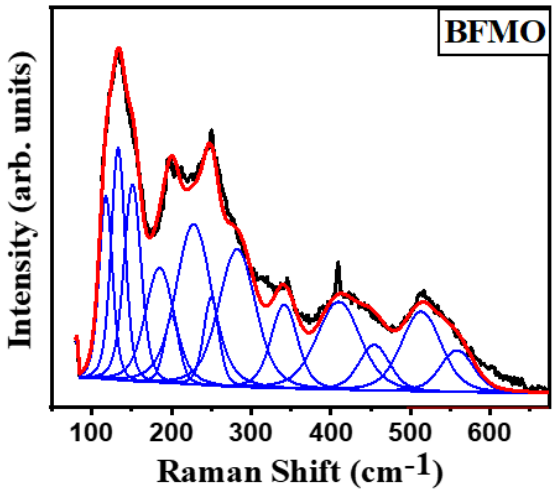

Figure 3.11: Raman spectra of Mn^{+3} substituted BFO thin films.

3.3.3.4 $Bi_{1-x}La_xFe_{1-y}Mn_yO_3$

The Raman spectra of La and Mn co-substituted BFO sample is shown in figure 3.12. Raman spectra of co-substituted composition indicates that E1, E2 and A1 modes merge together, the intensity of these modes also observed to decrease as compared to BFO, BLFO and BFMO sample. La substituted in place of Bi effects the lower frequency modes because these modes correspond to the bond vibration of A-site dopant with Oxygen while, Mn^{+3} substitution in place of Fe^{+3} effects the bond vibrations of the modes observed at higher frequencies. Broadness of the peaks and change in their intensities is an indication that some other structural phase also exists along with the rhombohedral phase. This result also agrees with the XRD analysis which also confirms the presence of mixed phase in co-substituted BFO sample.

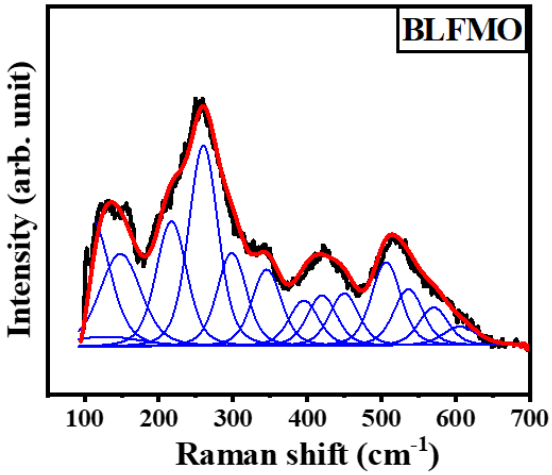

Figure 3.12: Raman spectra of co-substituted BFO thin films.

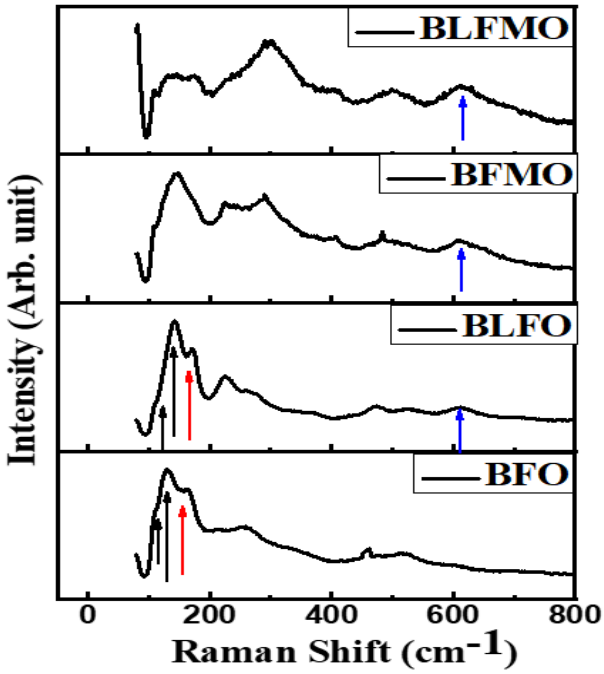

Figure 3.13: Comparison between observed Raman mode positions for doped and un-doped compositions (cm^{-1}).

Raman mode frequency depends on the factor $\sqrt{\frac{k}{\mu}}$ (where k is spring constant and μ is the reduced mass). Substitution of lower atomic weight of La^{+3} (138.90 g) as compared with the atomic weight of Bi^{+3} (208.98 g) affects the Raman modes [12]. From figure 3.14 it is observed that La and Mn substituted BFO sample indicate the similar modes as observed in pure BFO while, co-substituted

BFO sample indicate the presence of some new modes. These results are consistent with the XRD analysis. Position of the Raman modes of all the four samples are summarized in table 3.8.

Table 3.8: Comparison between observed Raman mode positions for doped and un-doped compositions (cm^{-1}).

Raman Modes(cm^{-1})	**$BiFeO_3$**	**$Bi_{1-x}La_xFeO_3$**	**$BiFe_{1-y}Mn_yO_3$**	**$Bi_{1-x}La_xFe_{1-y}Mn_yO_3$**
E-1	109.98	122.33	117.50	116.09
E-2	122.98	133.10	133.88	147.51
A_1-1	147.81	153.62	150.98	217.31
A_1-2	179.47	156.70	187.03	260.73
E-3	222.12	191.07	201.71	298.08
A_1-3	274.61	209.71	230.35	345.80
E-4	311.44	235.19	250.86	396.93
E-5	355.93	271.44	282.78	418.12
E-6	389.75	311.79	341.77	449.69
A_1-4	411.58	357.96	411.30	507.48
E-7	439.24	400.20	453.05	535.64
E-8	463.07	447.22	515.17	571.36
E-9	484.90	518.02	559.34	603.67

Chapter 4 Results and Discussion

The results of optical properties of Pure, La and Mn doped, and La-Mn co-doped BFO thin films will be discussed in this chapter.

4.1 UV-Vis SPECTROSCOPY

The optical response of pure BFO, La^{3+} doped, Mn^{3+} doped and La^{3+} and Mn^{3+} co-doped BFO thin film compositions will be discussed in this section.

4.1.1 Optical response of Pure BFO

In figure 4.1, diffused reflectance spectra of pure BFO are shown. Where Kubelka-Munk (KM) function is

$$F(R) = \frac{1 - R^2}{2R}$$

is plotted as a function of energy to calculate the band gap. In the KM plots of pure BFO four distinct shoulders are detected, as shown in figure 4.1. In the deformed FeO_6 octahedral symmetry (C_{3v}) which is created by the crystal ligand field, the first two shoulders appear due to Fe^{3+} at 1.79 eV and 2.44 eV that corresponds to the transitions of $^6A_{1g} \rightarrow {}^4T_{1g}$ and $^6A_{1g} \rightarrow {}^4T_{2g}$. These transitions of Fe^{3+} are called as *d-d₁* and *d-d₂* transitions and arise due to Fe^{+3} in distorted FeO_6 octahedral symmetry (i.e., C_{3v}) produced by crystal ligand field [72]. The absorption spectra of BFO significantly increases after 2.46 eV, with the third shoulder appear at 2.82 eV and last shoulder appearing at 3.29 eV. These transitions are termed as charge transfer (CT)[73, 74]. Third shoulder which is appear at 2.8 eV, occur due to transition between two distinct Fe ions i.e., Fe_1-3d - Fe_2-3d and labeled as CT transition whereas the shoulder of O_{2p} - Fe_{3d} and O_{2p} -Bi_{6s} CT transition lie around 3.3 eV and 4.2 eV [75]. In pure BFO, band gap is formed because of the overlapping of 2*p* oxygen and iron 3*d* levels [48].

The point group symmetry breakdown occurs between Oh and C_{3v} due to the distorted rhombohedral structure of the pure BFO thin film. It is expected that all the d-d transitions are present between 0-3 eV [76]. First two shoulders lie between 1.8 to 2.5 eV and these correspond to the excitation of $6A_{1g} \rightarrow 4A_{1g}$ and $6A_{1g} \rightarrow 4A_{2g}$. Such transition is labelled as *d-d* field crystal excitations of Fe^{3+} in BFO [75].

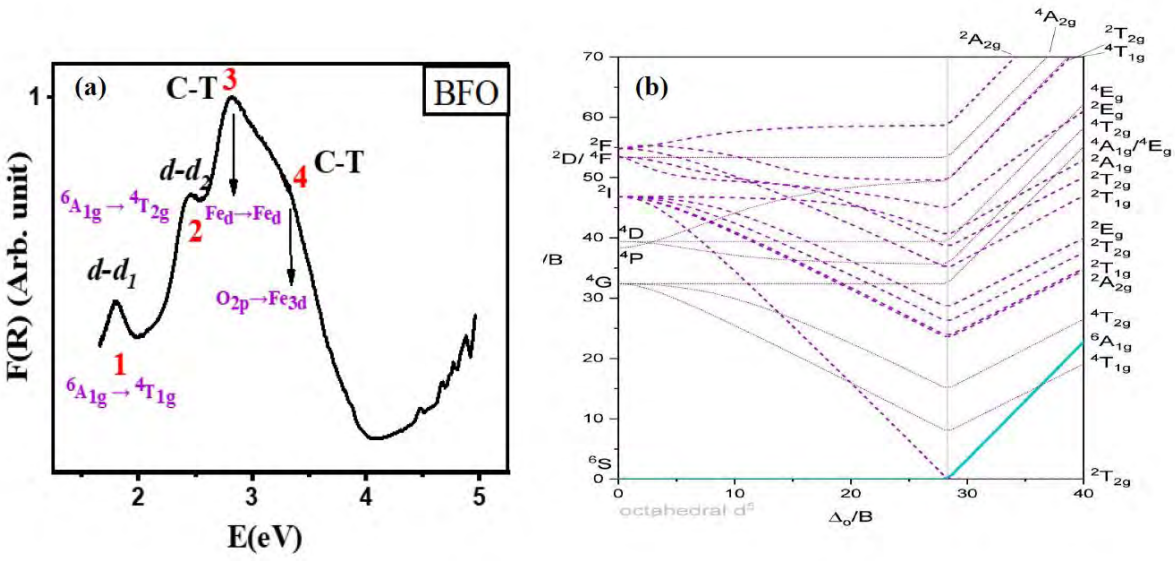

Figure 4.1:(a) Diffused reflectance spectra of pure BFO thin film at room temperature (b) d^5 transition.

4.3 Calculation of Band Gap

In order to determine the bandgap, the Kubelka-Munk function, F(R) = $\frac{1-R^2}{2R}$, is plotted as a function of energy. Direct bandgap can be computed by plotting a graph between $(E \times (R))^2$ and energy (E). By foreseeing the linear portion of the curve, one may determine the bandgap. The direct bandgap's value can be found by looking at the x-intercept of anticipated line. [15]. The direct bandgap of un-doped BFO composition is calculated to be equal to 2.08 eV. When it comes to BFO, the valence band is typically made up of 2p states of oxygen, whereas the conduction band is frequently made up of d-orbitals of Fe^{3+} [77].

4.3.1 Calculation of Racah parameters

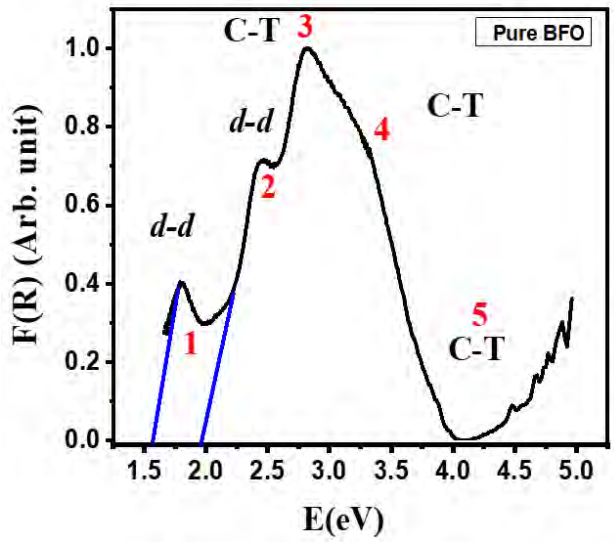

Figure 4.2: UV–visible reflectance spectra of $BiFeO_3$.

To further relate the experimental data with the theoretical calculations TS model is used and discussed in detail. To calculate the Racah parameter, crystal field splitting energy, and nephelauxetic ratio, TS diagrams are used for d^5 configuration of Fe^{3+} in $BiFeO_3$ as shown in figure 4.2. In an octahedral environment, the ligand approaches the central metal ion causing d-orbital splitting. This splitting is also known as crystal field splitting and is represented by the symbol Δ. The extent of overlapping between orbitals of Fe-3d and O-2p in the FeO_6 octahedra determine d-d transition energies [78]. From the experimentally calculated optical data two *d-d* transitions are observed in pure BFO. The first two transitions which corresponds to d-d transition are observed at energies of 1.564 eV and the other band at 1.97 eV as shown in figure 4.2.

We have $E_1 = 1.564\ eV$

$$E_1 = \frac{1.24*10^3}{\lambda_1}$$

Using the value of E_1, λ_1 becomes

$$\lambda_1 = 794\ \text{nm}$$

Similarly, for $E_2 = 1.97\ eV$, we get,

$$\lambda_2 = 629\ \text{nm}$$

Using relation $\upsilon = \frac{1}{\lambda \times 10^2}$

By putting the values of wavelength, we get

$$\upsilon_1 = 12594\ \ cm^{-1} \text{ and } \upsilon_2 = 15898\ \ cm^{-1}$$

E_1 and E_2 can be compared as

$$\frac{E_2}{E_1} = \frac{15898}{12594} = 1.26$$

Now, slide the ruler over Tanabe Sugano diagram (printed diagram) for d^5 complexes until the ratio of E_2/B_2 to E_1/B_1 or the ratio between the lines corresponding to the first two spin-allowed transitions becomes equivale to 1.26. In our case, this becomes 1.26 when $\frac{\Delta_o}{B} = 12$. At this moment find out the values of $\frac{E_2}{B_2}$ and $\frac{E_1}{B_1}$ by stopping the ruler. These ratios from TS diagram we get:

$$\frac{E_1}{B_1} = 22.5, \qquad \frac{E_2}{B_2} = 28.5$$

Where B_1 and B_2 are Racah Parameters. It is defined as the effect of electron-electron repulsion within the metal complexes for first and second transition. From the above relation the Racah parameters $B_1 = 559\ cm^{-1}$ and $B_2 = 557.8\ cm^{-1}$. By averaging B_1 and B_2, the Racah parameter is determined to be $558.4\ cm^{-1}$. Racah Parameter can be used to calculate the crystal field splitting energy Δ_o as

$$B_1 = \frac{12594\ cm^{-1}}{22.5} = 559\ \ cm^{-1}$$

$$B_2 = \frac{15898\ cm^{-1}}{28.5} = 557.8\ \ cm^{-1}$$

Their average value is B = $558.4\ cm^{-1}$

Crystal field splitting energy Δ_o is

$$\frac{\Delta_o}{B} = \frac{\Delta_o}{558.4} = 12$$

$$\Delta_o = 6{,}700\ cm^{-1}$$

Furthermore, we need to know the Racah parameter value for a free metal ion in its gaseous state in order to compute the nephelauxetic ratio. The value of B for the free (d^5) Fe^{+3} ion is $814\ cm^{-1}$. Hence, the nephelauxetic ratio β is

$$\beta = \frac{B_{complex}}{B_{free\ ion}} = \frac{558.4}{814} = 0.685$$

Experimental data have also been compared with theoretical density of states calculations reported in order in literature. The electronic configuration of Fe^{3+} is $3d^6 4s^2$ in FeO_6 octahedra. Three electrons contributes in the Fe^{3+} electronic state, two from 4s orbit and one from 3d orbit to be hybridized with the one unpaired electron of O-2p. 2s and 2p orbitals of oxygen in FeO_6 octahedra hybridized with Fe 3d, 4s, and 4p when ligand oxygen approaches the central metal ion. Due to crystal field splitting, Fe 3d orbitals in an octahedral environment break into (doublet state) and (triplet state) orbitals, as shown in figure 4.3. T_{2g} orbitals have less energy in this symmetry than e_g orbitals. Fe^{3+} has a spherically symmetric 4s orbital, which is denoted by the symbol A_{1g}. While the T1u represents the Fe^{3+} 4p orbitals. Fe's 4s, 4p, and 3d states are hybridized to produce the A_{1g}, e_g, T_{1g}, T_{2g}, T1u, and T_{2u} levels represented in figure 4.3. *d-d* transitions indicate the electronic transitions between these states. Required possible hybridized states are displayed along with their related electronic d-d transitions are shown in figure 4.3, and two possible *d-d* transitions between these hybridized states are are denoted as 1 and 2. Similar to this, the sp state hybridized by s and P_z states are combined in oxygen forming $\boldsymbol{\sigma}$ bond, while the s state produces a π bond when the s state is combined with the P_x and P_y states resulting sp state. Thus, in FeO_6 octahedra, six oxygen s orbitals (s hybridization with P_z) and twelve oxygen s orbitals (s hybridization with P_x and P_y) are created. A_{1g}, T_{1u}, and e_g represent six orbitals in this case. While twelve π orbitals are represented by T_{1g}, T_{2g}, T_{1u}, and T_{2u} [79]. Fe-3d and Bi-6s states make only a slight contribution to the valence band, which is primarily filled by O-2p states [74, 79-81]. Bi-6s states occupy the lower portion of the valence band from -9 eV to about -11 eV. O-2p states, with a negligible contribution from Fe-3d states, account for the majority of the valence band's top region from -6.9 to 0 eV. The conduction band above the bandgap is also affected by the Fe-3d states that are present in the valence band. Above the Fermi level, the region surrounding the conduction band minima (between 2.5 and 4 eV) is primarily filled by Fe-3d states, with a little contribution from O-2p states. Bi-6p states mainly occupy the conduction band's middle region (from 6 to 8 eV), whereas Fe-4s states are found in the region between 10 and 11 eV [74, 79-81] . Due to the polar nature of the Fe-O bond, O-2p states are primarily found in the valence band, whereas Fe-3d states are usually found in the conduction band. The bandgap of BFO is found between these two states as shown in figure 4.3.

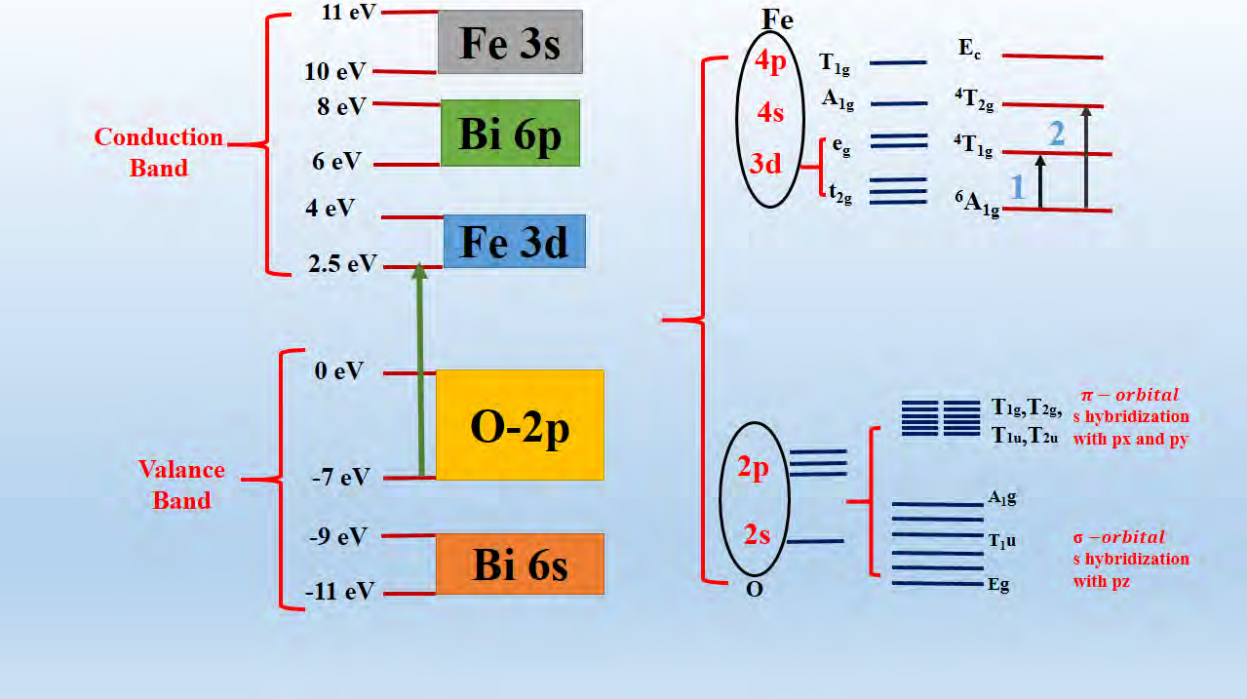

Figure 4.3: Schematic diagram of energy levels present in valence and conduction band in pure BFO compositions.

4.4 Optical response of La^{3+} substituted BFO thin films

At room temperature the diffused reflectance spectra of La^{3+} doped BFO thin films is shown in figure 4.4. KM plots show four distinct shoulders of La^{3+} doped BFO thin films which was observed for pure BFO as well, as seen in figure 4.4. It is observed from XRD analysis that when La^{3+} ($x = 0.05$) is substituted in BFO, then no structural transformation is observed. Therefore, no difference in the optical data is observed and similar four shoulders are observed as observed in pure BFO sample. Band gap is also calculated for BLFO sample and observed that it is less than pure BFO as shown in figure 4.4. It is because of La^{+3} orbitals existing in valence band -1.2 to -3.4 eV and in conduction band from 2.8 to 3.4 eV as shown in figure 4.4. Therefore, due to the existence of some new states in valance and conduction band in the region of band gap, its value decreases.

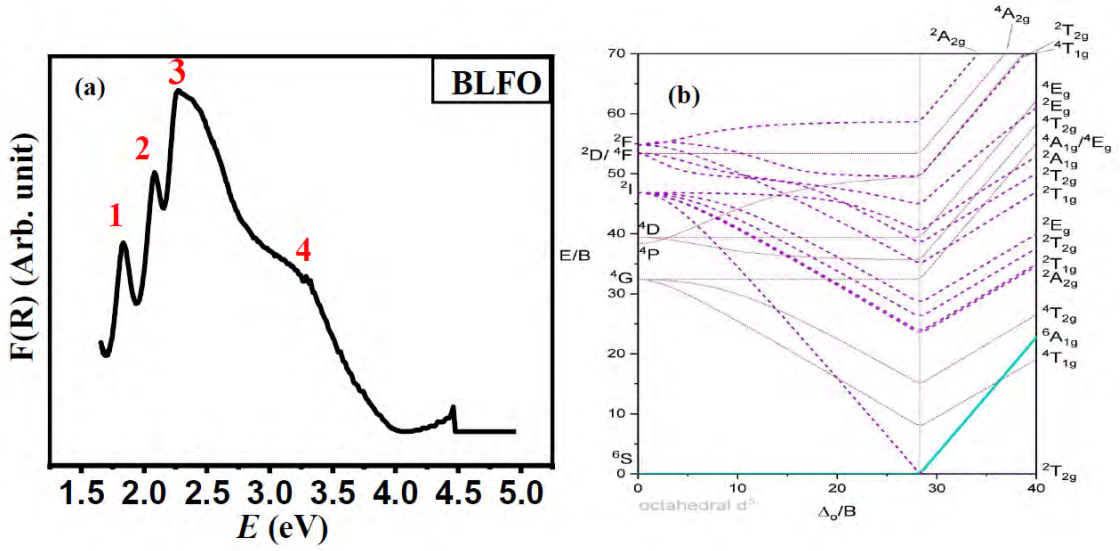

Figure 4.4: (a) UV–visible reflectance spectra of $Bi_{0.95}La_{0.05}FeO_3$ (b) d^5 transition.

At energies of 12822.65 cm^{-1} first two bands are seen and the other two are seen at 16048.53 cm^{-1}.We have

$$E_1 = 1.59 \text{ eV and } E_2 = 1.90 \text{ eV}$$

Using E$_1$ λ_1 will become

$$\lambda_1 = 779.87\ nm \text{ and } \lambda_2 = 623.11\ nm$$

So,

$$\upsilon_1 = 12822.65\ cm^{-1} \text{ and } \upsilon_2 = 16048.53\ cm^{-1}$$

E_1 and E_2 can be compared as

$$\frac{E_2}{E_1} = \frac{12822.65}{16048.53} = 1.19$$

Now, slide the ruler over Tanabe Sugano diagram (printed diagram) for d^5 complexes until the ratio of E$_2$/B to E$_1$/B or the ratio between the lines corresponding to the first two spin-allowed transitions becomes equivalent to 1.19. In our case, this becomes 1.19 when $\frac{\Delta_o}{B} = 13$.

The average value of Racah Parameter is B= 560 cm^{-1} and $\frac{\Delta_o}{B} = \frac{\Delta_o}{560} = 13$,

so

$$\Delta_o = 7280\ cm^{-1}.$$

Furthermore, we need to know the Racah parameter value for a free metal ion in its gaseous state in order to compute the nephelauxetic ratio. The value of B for the free free (d^5) Fe^{+3} ion is equal to 814 cm^{-1}. Hence, the nephelauxetic ratio β is

$$\beta = \frac{B_{complex}}{B_{free\ ion}} = \frac{560}{814} = 0.688$$

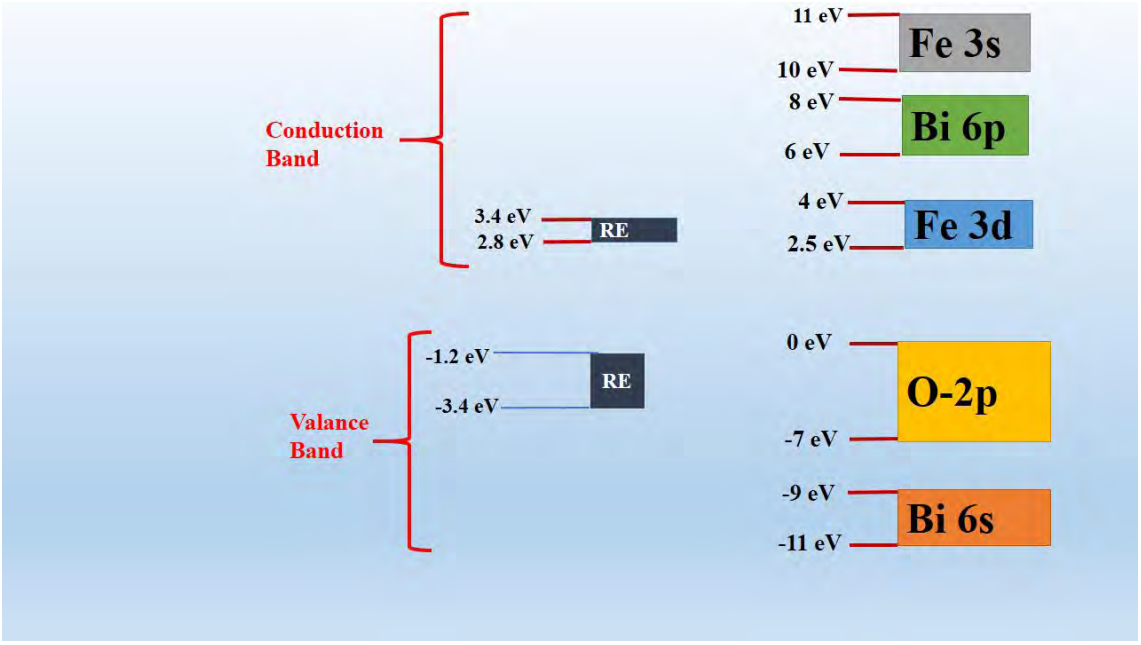

Figure 4.5: Schematic diagram of energy levels present in valence and conduction band in La doped BFO compositions.

4.5 Optical response of Mn^{3+} substituted BFO thin films

The diffused reflectance spectra of Mn^{3+} doped BFO thin films at room temperature is shown in figure 4.6. KM plots show four distinct shoulders of Mn^{3+} doped BFO thin films which was observed for pure BFO as well. It is observed from XRD analysis that when x = 0.025 amount of Mn^{3+} is substituted then no change results in structural transformation. In XRD analysis, same results was obtained i.e. structure retain its rhombohedral structure. Obtained value of band gap is found to be 1.64 eV which is less than band gap value of BFO. Now for the calculation of parameters we find two energy points from reflectance graph.

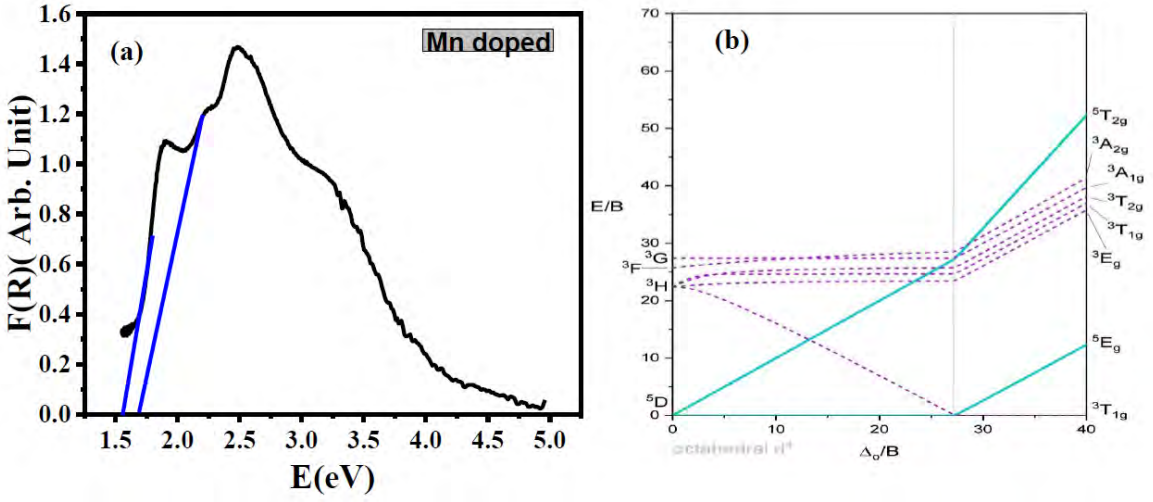

Figure 4.6: (a) UV–visible reflectance spectra of Mn doped $BiFeO_3$ (b) d^4 transition.

When Manganese (Mn^{+3}) is doped at B site of pure BFO ($BiFeO_3$). The electronic configuration for Mn^{+3} becomes $3d^4$. Now by using Tanabe Sugano diagram for $3d^4$ configuration number of allowed transitions are only one that is ^5E_g to $^5T_{2g}$

$$E_1 = 1.564\ eV$$

$$E_1 = \frac{1.24X10^3}{\lambda 1}$$

Put the value of E_1 in equation, we get

$$\lambda_1 = 792\ nm$$

We have a relation $\upsilon = \frac{1}{\lambda \times 10^2}$ so $\upsilon_1 = 12626\ cm^{-1}$

$$E_1 = 12636\ cm^{-1}$$

$$\frac{\Delta_o}{B} = 25$$

$$B = 505\ cm^{-1}$$

Furthermore, we need to know the Racah parameter value for a free metal ion in its gaseous state in order to compute the nephelauxetic ratio. The value of B for the free Mn^{+3} ion is equal to 860 cm^{-1}. Hence, the nephelauxetic ratio β is

$$\beta = \frac{Bcomplex}{Bfree\ ion} = \frac{505}{860} = 0.58$$

It is because the size of Mn^{+3} ions (0.72 Å) is greater than that of Fe^{+3} (0.69 Å).

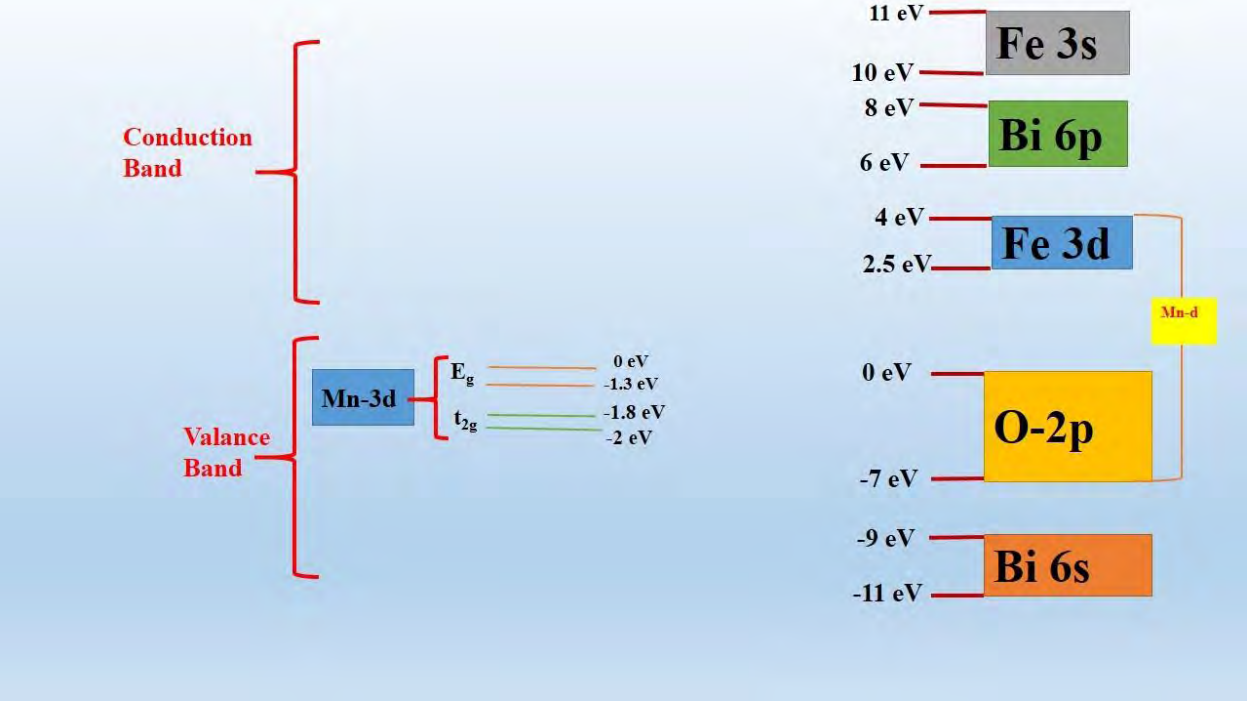

Figure 4.7: Schematic diagram of energy levels present in valence and conduction band in Mn doped BFO compositions.

Here 100% overlap of Mn-3d and O-2p orbitals occur which then effect d-d transition i.e. one transition corresponds to Fe-3d is removed and another transition is appeared due transition between different states of O and Mn 3d states as shown in figure 4.7.

4.6 Optical response of La^{3+} and Mn^{3+} co-substituted BFO thin films

Diffused reflectance spectra of La^{+3} and Mn^{+3} co-substituted BFO thin films are presented in figure 4.8. It is observed from the figure that one of the *d-d* transitions vanishes in the La-Mn co-doped thin film composition. XRD analysis indicates the presence of mixed rhombohedral and cubic phase so vanishing of *d-d* transition indicates that co-substitution of dopant at A and B-site trigger the structure towards centrosymmetric phase. According to Laporte rule *d-d* transition is forbidden in centrosymmetric configuration. Band gap value reduces further to 1.52 eV. It is

helpful for photovoltaic and photocatalytic response when band-gap values of co-doped BFO samples are lowered since this causes good wide-spectrum light absorption.

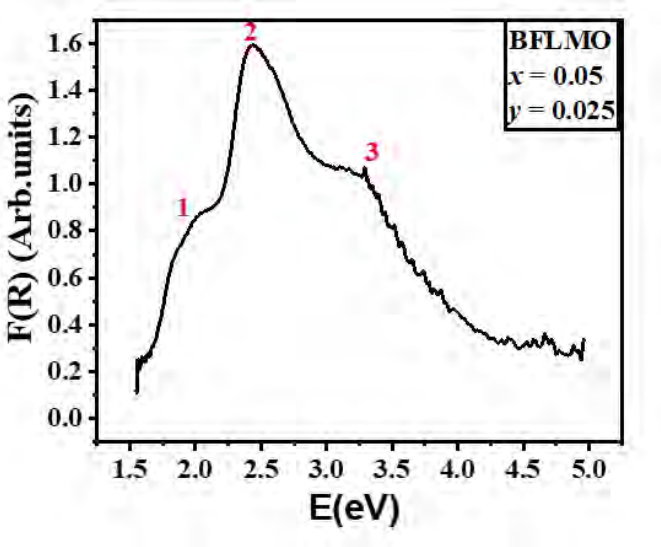

Figure 4.8: Diffused reflectance spectra of La (x = 0.05) and Mn (y = 0.025) co-doped BFO thin films.

Substitution of Mn in $Bi_{1-x}La_xFeO_3$ thin films reduces very small band gap as shown in figure 4.8. It is because of Mn^{+3} ion substitution for the same valence of Fe ion which form the donor impurity energy levels. Only one peak corresponds to Fe-3d appeared.

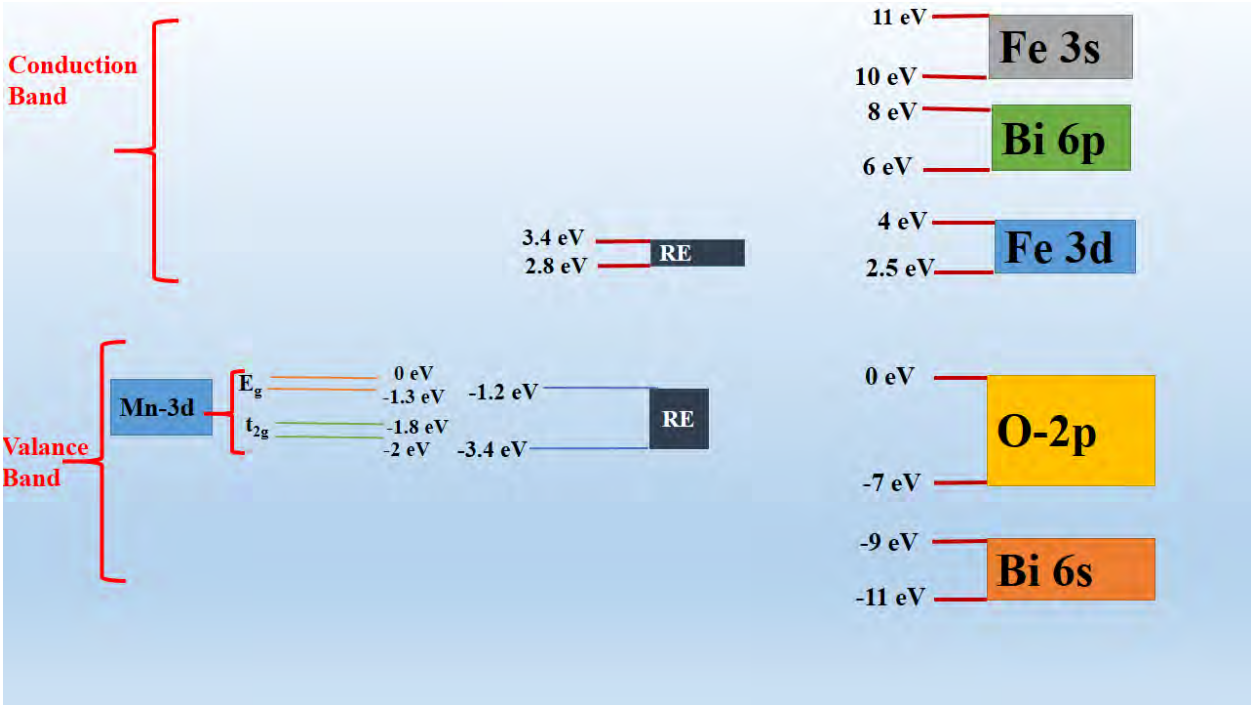

Figure 4.9: Schematic diagram indicating the energy levels present in valance and conduction band in pure, substituted, and co-substituted BFO compositions.

In literature, the density of states calculated for $LaFeO_3$ lies between -3.4 eV to -1.2 eV in valence band and 2.8 eV to 3.4 eV conduction band. The conduction bands are mainly from Fe-3d and rare earth 4f states and valence bands that are present between 6 eV and 0 eV originate from O 2p and Fe 3p states with a mixture of some rare-earth 5p-6s states. Filled O-2p states are located between 6 and 0 eV. The filled rare earth states are present between − 3.4 and − 1.2 eV, while the empty states lie between 2.8 and 3.4 eV. The empty states are located between 2.49 and 2.93 eV while the filled Fe e_g states are between 0.85 and 0.0 eV. The empty Fe t_{2g} states are located between 3.37 and 3.88 eV. The rare earth states are present in both valence and conduction bands resulting from theoretical calculation. Sai Gong et al. reported atomic DOSs between −6.5 and 4 eV calculated. Value of Mn e_g is -2 to -1.8 eV and for t_{1g} is -1.3 to 0 eV. The density of states of $LaFeO_3$ was reported by Rajan et al [82]. They also show that there is a hybridization between the Fe and La d states, with O-2p states at the top of the valence band and La and Fe 3d hybridized states at the bottom of the conduction band. Hence, due to the presence of hybridization between different states of Fe, La and Mn with O band gap value further reduces.

4.7 Conclusion

In present research, pure, substituted $Bi_{1-x}La_xFeO_3(x = 0.05)$, $BiFe_{1-y}Mn_yO_3(y = 0.025)$ and $Bi_{1-x}La_xFe_{1-y}Mn_yO_3(x = 0.05, y = 0.025)$ compositions are used. By using diol method $BiFeO_3$ (BFO) thin films were fabricated on FTO glass substrate using spin coating method. To obtain the pure perovskite phase, the synthesis procedure undergone further refining. Detailed structural analysis is done using X-ray diffractometer. Pure BFO having rhombohedral perovskite structure is being studied. Due to Bi volatilization synthesis of pure BFO thin films various issues have been reported. This results in the production of oxygen vacancies and impurity phases. Various dopants replaced at the BFO's A and B sites modulate the Bi volatilization. La and Mn have been substituted on A-site and B-site in pure BFO for this purpose. Chemical pressure and strain are caused by an ionic radii mismatch between the host and substituted ions in the system. This is then shifted the phase from rhombohedral to mixed phase in co-substituted BFO thin film composition. Results from Raman analysis are in agreement with XRD analysis and show broadening and merging of Raman modes, which supports the structural alteration in co-doped composition. At standard temperature,

optical spectra of pure and substituted thin film samples have been recorded. Decrease in bandgap was observed with substitution of dopant at A-site and B-site correspondingly, are observed in all the prepared thin film samples.

References

1. Chiu, F.-C. and C.-M.J.J.o.P.D.A.P. Lai, *Optical and electrical characterizations of cerium oxide thin films.* 2010. **43**(7): p. 075104.
2. Kao, K.C., *DIELECTRIC PHENOMENA IN SOLIDS.* ELSEVIER ACADEMIC PRESS, 2004. **2**(1): p. 601.
3. Zhang, F. and T.J.P.R.B. Rice, *Effective Hamiltonian for the superconducting Cu oxides.* 1988. **37**(7): p. 3759.
4. Gerra, G., et al., *Ionic polarizability of conductive metal oxides and critical thickness for ferroelectricity in BaTiO 3.* 2006. **96**(10): p. 107603.
5. Tomioka, Y., et al., *Collapse of a charge-ordered state under a magnetic field in Pr 1/2 Sr 1/2 MnO 3.* 1995. **74**(25): p. 5108.
6. Taz, H., et al., *Integration of amorphous ferromagnetic oxides with multiferroic materials for room temperature magnetoelectric spintronics.* 2020. **10**(1): p. 3583.
7. Chen, W., et al., *Two-dimensional Janus transition metal oxides and chalcogenides: multifunctional properties for photocatalysts, electronics, and energy conversion.* 2018. **10**(41): p. 35289-35295.
8. Vopson, M.M.J.C.R.i.S.S. and M. Sciences, *Fundamentals of multiferroic materials and their possible applications.* 2015. **40**(4): p. 223-250.
9. Bibes, M. and A.J.N.m. Barthélémy, *Towards a magnetoelectric memory.* 2008. **7**(6): p. 425-426.
10. Catalan, G. and J.F.J.A.m. Scott, *Physics and applications of bismuth ferrite.* 2009. **21**(24): p. 2463-2485.
11. Lawes, G. and G.J.J.o.P.D.A.P. Srinivasan, *Introduction to magnetoelectric coupling and multiferroic films.* 2011. **44**(24): p. 243001.
12. Agarwal, A., et al., *Structural and multiferroic properties of barium substituted bismuth ferrite nanocrystallites prepared by sol–gel method.* 2017. **426**: p. 800-805.
13. Gómez-Salces, S., et al., *Effect of pressure on the band gap and the local FeO 6 environment in BiFeO 3.* 2012. **85**(14): p. 144109.
14. Cooper, S.L., et al., *Localized to itinerant electronic transition in perovskite oxides*. Vol. 98. 2003: Springer.
15. Hussain, S., S.J.J.o.A. Hasanain, and Compounds, *Chemical pressure induced red shift in band gap and dd transition energies in Sr doped BiFeO3.* 2016. **688**: p. 1151-1156.
16. Atkins, P., *Shriver and Atkins' inorganic chemistry*. 2010: Oxford University Press, USA.
17. Mohapatra, L., K.J.C.S. Parida, and Technology, *A review of solar and visible light active oxo-bridged materials for energy and environment.* 2017. **7**(11): p. 2153-2164.
18. Kao, K.C., *Dielectric phenomena in solids*. 2004: Elsevier.
19. Setter, N. and E. Colla, *Ferroelectric ceramics: tutorial reviews, theory, processing, and applications*. 1993: Springer.
20. Khan, M.I. and T.C.J.M.F.M. Upadhyay, *General Introduction to Ferroelectrics.* 2021: p. 7.
21. Thouless, D.J.A.J.o.P., *Magnetism in condensed matter by Stephen Blundell.* 2003. **71**(1): p. 94-94.
22. Fiebig, M., T.J.O.o.c.m. Lottermoser, and e. domains, *GOLTSEv A v, PISAREv R V.* 2002. **419**: p. 818-820.

23. Spaldin, N.A. and R.J.N.m. Ramesh, *Advances in magnetoelectric multiferroics.* 2019. **18**(3): p. 203-212.
24. Martin, L., et al., *Advances in the growth and characterization of magnetic, ferroelectric, and multiferroic oxide thin films.* 2010. **68**(4-6): p. 89-133.
25. Palneedi, H., et al. *Status and perspectives of multiferroic magnetoelectric composite materials and applications*. in *Actuators*. 2016. MDPI.
26. Ortega, N., et al., *Multifunctional magnetoelectric materials for device applications.* 2015. **27**(50): p. 504002.
27. Wang, N., et al., *Structure, performance, and application of BiFeO 3 nanomaterials.* 2020. **12**: p. 1-23.
28. Young, S.M., F. Zheng, and A.M.J.P.r.l. Rappe, *First-principles calculation of the bulk photovoltaic effect in bismuth ferrite.* 2012. **109**(23): p. 236601.
29. Fischer, P., et al., *Temperature dependence of the crystal and magnetic structures of BiFeO3.* 1980. **13**(10): p. 1931.
30. Hussain, S., et al., *Size and lone pair effects on the multiferroic properties of Bi 0.75 A 0.25 FeO 3− δ (A= Sr, Pb, and Ba) ceramics.* 2013. **96**(10): p. 3141-3148.
31. Yang, J.-C., et al., *BiFeO3 thin films: a playground for exploring electric-field control of multifunctionalities.* 2015. **45**: p. 249-275.
32. Seshadri, R. and N.A.J.C.o.m. Hill, *Visualizing the role of Bi 6s "lone pairs" in the off-center distortion in ferromagnetic BiMnO3.* 2001. **13**(9): p. 2892-2899.
33. Yang, C.-H., et al., *Doping BiFeO 3: approaches and enhanced functionality.* 2012. **14**(46): p. 15953-15962.
34. Wan, X., et al., *Ferroelectricity induced by interatomic magnetic exchange interaction.* 2012.
35. Neaton, J., et al., *First-principles study of spontaneous polarization in multiferroic Bi Fe O 3.* 2005. **71**(1): p. 014113.
36. Sando, D., et al., *Crafting the magnonic and spintronic response of BiFeO3 films by epitaxial strain.* 2013. **12**(7): p. 641-646.
37. Chu, Y.-H., et al., *Electric-field control of local ferromagnetism using a magnetoelectric multiferroic.* 2008. **7**(6): p. 478-482.
38. Chu, Y.-H., et al., *Controlling magnetism with multiferroics.* 2007. **10**(10): p. 16-23.
39. Dhir, G., P. Uniyal, and N.J.M.s.i.s.p. Verma, *Effect of particle size on multiferroism of barium-doped bismuth ferrite nanoparticles.* 2014. **27**: p. 611-618.
40. Rao, T.D., et al., *Structural and magnetic properties of Ba and Sn co-substituted bismuth ferrite.* 2021. **39**: p. 1515-1518.
41. Pani, T.K. and B.J.J.o.P.D.A.P. Sundaray, *A correlation of lattice distortion with the magnetic properties of calcium doped bismuth ferrite thin films.* 2021. **54**(20): p. 205002.
42. Bozgeyik, M.S., R.K. Katiyar, and R.S.J.J.o.E. Katiyar, *Improved magnetic properties of bismuth ferrite ceramics by La and Gd co-substitution.* 2018. **40**(3): p. 247-256.
43. Agarwal, A., et al., *Structural transitions and multiferrocity in Ba and Co substituted nanosized bismuth ferrite.* 2017. **697**: p. 333-340.
44. Jha, P.K., et al., *Sm/Ti co-substituted bismuth ferrite multiferroics: reciprocity between tetragonality and piezoelectricity.* 2017. **19**(38): p. 26285-26295.
45. Rojac, T., et al., *BiFeO 3 ceramics: processing, electrical, and electromechanical properties.* 2014. **97**(7): p. 1993-2011.

46. Qi, X., et al., *Greatly reduced leakage current and conduction mechanism in aliovalent-ion-doped BiFeO3.* 2005. **86**(6).
47. Wang, J., et al., *Epitaxial BiFeO3 multiferroic thin film heterostructures.* 2003. **299**(5613): p. 1719-1722.
48. Sharma, P., V.J.J.o.M. Verma, and M. Materials, *Structural, magnetic and electrical properties of La and Mn co-substituted BFO samples prepared by the sol–gel technique.* 2015. **374**: p. 18-21.
49. Yan, F., et al., *In situ synthesis and characterization of fine-patterned La and Mn co-doped BiFeO3 film.* 2013. **570**: p. 19-22.
50. Wang, Y., et al., *Room-temperature ferromagnetism in Fe-doped Na0. 5Bi0. 5TiO3 crystals.* 2009. **27**: p. 471-476.
51. Chauhan, S., et al., *Multiferroic, magnetoelectric and optical properties of Mn doped BiFeO3 nanoparticles.* 2012. **152**(6): p. 525-529.
52. Dhanalakshmi, B., et al., *Enhanced magnetic and magnetoelectric properties of Mn doped multiferroic ceramics.* 2017. **43**(12): p. 9272-9275.
53. Yan, X., et al., *Structural, electric and magnetic properties of Dy and Mn co-doped BiFeO3 thin films.* 2015. **41**(2): p. 3202-3207.
54. Kumar, M. and K.J.J.o.P.C.M. Yadav, *The effect of Ti substitution on magnetoelectric coupling at room temperature in the BiFe1− xTixO3 system.* 2006. **18**(40): p. L503.
55. Wang, Y., et al., *Promoted photocarriers separation by straining in 2D/2D van der Waals heterostructures for high-efficiency visible-light photocatalysis.* 2022. **22**: p. 100600.
56. Das, R., T. Sarkar, and K.J.J.o.P.D.A.P. Mandal, *Multiferroic properties of Ba2+ and Gd3+ co-doped bismuth ferrite: magnetic, ferroelectric and impedance spectroscopic analysis.* 2012. **45**(45): p. 455002.
57. Yu, B., et al., *Enhanced electrical properties in multiferroic BiFeO3 ceramics co-doped by La3+ and V5+.* 2008. **41**(18): p. 185401.
58. HON'BLE, M., et al., *The Roster of sitting of Hon'ble the Acting Chief Justice and Hon'ble Judges wef 02.01. 2012 shall be as under: NAME OF HON'BLE JUDGES COURT NO.*
59. Xi, X., et al., *Enhanced magnetic and conductive properties of Ba and Co co-doped BiFeO3 ceramics.* 2014. **355**: p. 259-264.
60. Fiebig, M.J.J.o.p.D.a.p., *Revival of the magnetoelectric effect.* 2005. **38**(8): p. R123.
61. Khomchenko, V., et al., *Effect of diamagnetic Ca, Sr, Pb, and Ba substitution on the crystal structure and multiferroic properties of the BiFeO3 perovskite.* 2008. **103**(2).
62. Cheng, C.-J., et al., *Microstructure-electromechanical property correlations in rare-earth-substituted BiFeO3 epitaxial thin films at morphotropic phase boundaries.* 2010. **97**(21).
63. Singh, S., K. Maruyama, and H.J.A.P.L. Ishiwara, *Reduced leakage current in La and Ni codoped BiFeO3 thin films.* 2007. **91**(11).
64. Cheng, G., et al., *Structural phase transition and thermal expansion in Bi1− 2.5 xPr1. 5xBaxFeO3 ceramics.* 2013. **566**: p. 235-238.
65. Ravindran, P., et al., *Theoretical investigation of magnetoelectric behavior in Bi Fe O 3.* 2006. **74**(22): p. 224412.
66. Pugaczowa-Michalska, M. and J.J.J.o.m.s. Kaczkowski, *First-principles study of structural, electronic, and ferroelectric properties of rare-earth-doped BiFeO 3.* 2015. **50**: p. 6227-6235.
67. Reddy, V.A., N.P. Pathak, and R.J.S.s.c. Nath, *Enhanced magnetoelectric coupling in transition-metal-doped BiFeO3 thin films.* 2013. **171**: p. 40-45.

68. Nikitenkov, N., *Modern Technologies for Creating the Thin-film Systems and Coatings*. 2017: BoD–Books on Demand.
69. Damay, F., et al., *Spin-lattice coupling induced phase transition in the S= 2 frustrated antiferromagnet CuMnO 2.* 2009. **80**(9): p. 094410.
70. Wu, Y.-J., et al., *Magnetic enhancement across a ferroelectric–antiferroelectric phase boundary in Bi1− xNdxFeO3.* 2012. **111**(5).
71. Garcia, F.G., et al., *Lanthanum doped BiFeO3 powders: Syntheses and characterization.* 2010. **501**(1): p. 25-29.
72. Xu, X., et al., *Optical properties and magnetochromism in multiferroic BiFeO 3.* 2009. **79**(13): p. 134425.
73. Pisarev, R., et al., *Charge transfer transitions in multiferroic BiFeO 3 and related ferrite insulators.* 2009. **79**(23): p. 235128.
74. Clark, S. and J.J.A.p.l. Robertson, *Band gap and Schottky barrier heights of multiferroic BiFeO3.* 2007. **90**(13).
75. Mumtaz, F., et al., *Chemical pressure exerted by rare earth substitution in BiFeO3: Effect on crystal symmetry, band structure and magnetism.* 2021. **876**: p. 160178.
76. Reetu, R., et al., *Rietveld analysis, dielectric and magnetic properties of Sr and Ti codoped BiFeO3 multiferroic.* 2011. **110**(7).
77. Sheu, Y.-M., et al., *Ultrafast carrier dynamics and radiative recombination in multiferroic BiFeO3.* 2012. **100**(24).
78. Blundell, S., *Magnetism in condensed matter*. 2001: OUP Oxford.
79. Liu, K., et al., *Structural, electronic and optical properties of BiFeO3 studied by first-principles.* 2011. **509**(5): p. 1901-1905.
80. Gao, N., et al., *Experimental and first principles investigation of the multiferroics BiFeO3 and Bi0. 9Ca0. 1FeO3: structure, electronic, optical and magnetic properties.* 2016. **481**: p. 45-52.
81. Zhu, X.-H., et al., *Electronic structure, magnetism and optical properties of orthorhombic GdFeO 3 from first principles.* 2017. **7**(7): p. 4054-4061.
82. Iyyappa Rajan, P., et al., *High thermopower and power factors in EuFeO3 for high temperature thermoelectric applications: A first-principles approach.* 2020. **128**(15).